Bayesian analysis of azimuthal anisotropy in the Alpine lithosphere from beamforming of ambient noise cross-correlations

Dorian Soergel, Helle A Pedersen, Thomas Bodin, Anne Paul, Laurent Stehly

Geophysical Journal International

Geophys. J. Int. (2023) **232,** 429–450
Advance Access publication 2022 September 07
GJI Seismology

https://doi.org/10.1093/gji/ggac349

Bayesian analysis of azimuthal anisotropy in the Alpine lithosphere from beamforming of ambient noise cross-correlations

Dorian Soergel [1], Helle A. Pedersen [2], Thomas Bodin [1], Anne Paul,[2] Laurent Stehly[2] and AlpArray Working Group[†]

[1] *Univ Lyon, UCBL, ENSL, UJM, CNRS, LGL-TPE, F-69622, Villeurbanne, France. E-mail: soergeldorian@gmail.com*
[2] *Univ. Grenoble Alpes, Univ. Savoie Mont Blanc, CNRS, IRD, Univ. Gustave Eiffel, ISTerre,* 38000 *Grenoble, France*

Accepted 2022 August 25. Received 2022 August 22; in original form 2022 March 11

SUMMARY

Surface waves extracted from ambient noise cross-correlations can be used to study depth variations of azimuthal anisotropy in the crust and upper mantle, complementing XKS splitting observations. In this work, we propose a novel approach based on beamforming to estimate azimuthal anisotropy of Rayleigh wave phase velocities extracted from ambient noise cross-correlations. This allows us to identify and remove measurements biased by wave front deformation due to 3-D heterogeneities, and to properly estimate uncertainties associated with observed phase velocities. In a second step, phase velocities measured at different periods can be inverted at depth with a transdimensional Bayesian algorithm where the presence or absence of anisotropy at different depths is a free variable. This yields a comprehensive probabilistic solution that can be exploited in different ways, in particular by projecting it onto a lower dimensional space, appropriate for interpretation. For example, we show the probability distribution of the integrated anisotropy over a given depth range (e.g. upper crust, lower crust). We apply this approach to recent data acquired across the AlpArray network and surrounding permanent stations. We show that only the upper crust has a large-scale coherent azimuthal anisotropy at the scale of the Alps with fast axis directions parallel to the Alpine arc, while such large-scale patterns are absent in the lower crust and uppermost mantle. This suggests that the recent Alpine history has only overridden the anisotropic signature in the upper crust, and that the deeper layers carry the imprint of older processes. In the uppermost mantle, fast directions of anisotropy are oriented broadly north–south, which is different from results from XKS-splitting measurements or long-period surface waves. Our results therefore suggest that XKS observations are related to deeper layers, the asthenosphere and/or subduction slabs. The area northwest of the Alps shows strong anisotropy in the lower crust and uppermost mantle with a fast axis in the northeast direction that could be related to Variscan deformation.

Key words: Europe; Interferometry; Inverse theory; Probability distributions; Seismic anisotropy; Seismic interferometry.

1 INTRODUCTION

The Alpine area is part of the collision zone due to the convergence of the African and Eurasian plates. It involves a variety of microplates, leading to high amounts of deformation in the crust and a complex 3-D lithospheric geometry (Nocquet & Calais 2004; Handy *et al.* 2010). Knowledge of past and present stress and strain fields is key to better understand the history and evolution of the Alps and surrounding mountain belts (Handy *et al.* 2010; Faccenna *et al.* 2014). The present-day deformation and stress fields in the crust have been studied in the Alps using analysis of GNSS data and earthquake focal mechanisms (e.g. Delacou *et al.* 2004; Heidbach *et al.* 2018; Mathey *et al.* 2020). Seismic anisotropy provides complementary information on the history of deformation as stress and deformation directly affect the alignment of seismically anisotropic minerals, as well as lithospheric structures such as faults, fluids, layering, etc. (Backus 1962; Anderson *et al.* 1974; Kaminski & Ribe 2001; Jung & Karato 2001; Almqvist & Mainprice 2017).

Observationally, seismic anisotropy is generally divided into radial and azimuthal anisotropy, the former being the change of seismic velocity in the vertical plane and the latter in the horizontal plane. A recent study of radial anisotropy in the Alps showed that

[†] https://www.alparray.ethz.ch/

radial anisotropy is strong only in a few areas, and mainly limited to the crust (Alder *et al.* 2021). Azimuthal anisotropy in the Alps has mainly been measured using XKS-splitting data (e.g. Wüstefeld *et al.* 2009; Barruol *et al.* 2011; Bokelmann *et al.* 2013; Qorbani *et al.* 2015; Salimbeni *et al.* 2018; Hein *et al.* 2021). As those measurements use body waves propagating quasi-vertically, it is difficult to constrain the depth of the measured anisotropy. It is generally attributed to the upper mantle, as the crust has a much smaller thickness, even though it has been shown by Link *et al.* (2020) that it can influence the results of XKS measurements. Other phases such as Pn and Sn have also been used in the area to study azimuthal anisotropy (Meissner *et al.* 2002; Díaz *et al.* 2013), but these observations are difficult to interpret in an area with strong variations in Moho depth such as the Alps (Spada *et al.* 2013). Finally, receiver functions can resolve the average azimuthal anisotropy in the crust, but there is a trade-off with Moho dip, so that the stability of the method is at least partly dependent on precise knowledge of Moho geometry (e.g. Link *et al.* 2020).

Surface waves provide complementary information to XKS, because their depth penetration increases with period, and dispersion measurements are sensitive to depth variations. Similarly to XKS measurements, it is necessary to have velocity estimates over a good azimuthal coverage to reliably constrain the direction of fast wave propagation. The local seismicity generally does not provide sufficient azimuthal coverage, unless the entire area is very seismogenic, which is not the case for the wider alpine region. Also, the magnitudes of local and regional earthquakes in the area are generally small to moderate and therefore dominated by high frequency surface waves which do not sample the whole crust nor the upper mantle. The two possible sources of surface waves that provide good azimuthal coverage in the Alps are therefore either teleseismic events or ambient noise cross-correlations, which are increasingly used for imaging purposes in seismology, following the seminal works of Campillo & Paul (2003), Shapiro & Campillo (2004), Shapiro *et al.* (2005) and Sabra *et al.* (2005). The correlation approximates the Green's function, that is the waveform recorded at one station, if a point source was applied at the location of the other station. This latter station is referred to as a virtual source throughout this work. Here we use noise correlations in the period range 10–75 sonstrain azimuthal anisotropy in the crust and the uppermost mantle. The azimuthal coverage is excellent thanks to the dense station coverage of the study area and surrounding regions. Furthermore, ambient noise measurements suffer less than teleseismic data from multipathing, wave front deformations or great-circle deviations (e.g. Cotte *et al.* 2000; Tanimoto & Prindle 2007; Pedersen *et al.* 2015; Kolínský *et al.* 2019, 2020).

Surface waves obtained from noise cross-correlations in the Alps have already been used by Fry *et al.* (2010) to measure azimuthal anisotropy. They used a tomographic approach based on phase velocity measurements using the two-station method (e.g. Meier *et al.* 2004; Deschamps *et al.* 2008; Soomro *et al.* 2015), using relatively few stations in the Swiss Alps. Above 24 s period, they observed a north–south oriented fast direction of anisotropy at odds with the results from XKS measurements and a recent study by Kästle *et al.* (2021). The temporary seismic stations of the AlpArray project (Hetényi *et al.* 2018), for which station installation began in 2015, complements permanent networks installed in Europe, resulting in an approximately uniform coverage of the greater Alpine region with an interstation distance of approximately 50 km. There are therefore over 1000 seismic stations located in and around the Alps that can be used as virtual sources in a cross-correlation analysis (Fig. 1). Noise correlations in the greater Alpine region have already been the base of several studies of isotropic structure (e.g. Stehly *et al.* 2008; Lu *et al.* 2018b, 2020; Soergel *et al.* 2020; El-Sharkawy *et al.* 2020; Alder *et al.* 2021; Nouibat *et al.* 2022), and a single study focusing on azimuthal anisotropy (Kästle *et al.* 2021). At the local scale, azimuthal anisotropy of surface waves from noise correlations with AlpArray data has been studied in the Vienna basin by Schippkus *et al.* (2019).

Anisotropy measurements obtained from ambient noise cross-correlations remain challenging. First, the surface wave measurements need to overcome the same challenges as those based on teleseismic surface waves: the presence of 3-D heterogeneities can create an apparent anisotropy that does not correspond to the intrinsic anisotropy of the structure at depth (Bodin & Maupin 2008; Ritzwoller *et al.* 2011; Schippkus *et al.* 2019). Another challenge specific to ambient noise measurements is that the uneven distribution of noise sources can create biases in the recovered Green's function, and hence on measured velocities (e.g. Pedersen *et al.* 2007; Yao & van der Hilst 2009; Froment *et al.* 2010). These biases are mitigated by using beamforming and several years of data.

Once the empirical Green's functions are obtained from ambient noise cross-correlations, phase velocities remain the most natural choice to study azimuthal anisotropy because of ease of depth inversions (Montagner & Nataf 1986). Different methods can be used to extract the phase information, with different hypotheses and approximations. The two-station method (e.g. Meier *et al.* 2004) measures the phase velocity between pairs of stations for a given frequency, and then requires an inversion to obtain maps of phase velocity and azimuthal anisotropy by period. Another method used to obtain phase velocity measurements is eikonal tomography (Lin *et al.* 2009) and its extension Helmholtz tomography (Lin & Ritzwoller 2011). These methods rely on interpolating the traveltimes and using the gradient of the traveltime field to calculate the phase velocity in each point of the study area, for a given source. Combining several virtual sources, and therefore local velocity measurements from several directions, it is possible in any given point to calculate the variation of phase velocity with azimuth. Eikonal tomography has been applied by Lin *et al.* (2009) and Ritzwoller *et al.* (2011) and on the greater Alpine region by Kästle *et al.* (2021).

In this work, we implement an alternative approach based on beamforming to estimate azimuthal anisotropy of fundamental mode Rayleigh waves in noise correlations. Beamforming is now extensively used on raw ambient noise measurements to recover the location of noise sources (microseisms) (Gerstoft & Tanimoto 2007; Juretzek & Hadziioannou 2016; Retailleau & Gualtieri 2019). Using Beamforming to estimate azimuthal anisotropy has already been carried out on data from teleseismic events (Cotte *et al.* 2000; Tanimoto & Prindle 2007; Pedersen *et al.* 2015) and seismic noise correlations (Riahi *et al.* 2013; Riahi & Saenger 2014; Löer *et al.* 2018). We take a similar approach, and adapt the implementation to produce reliable results given the AlpArray station geometry and the specific challenges raised by the lateral heterogeneity of the Alps. The resulting anisotropy measurements at each period can then be inverted to constrain the depth variations of shear wave azimuthal anisotropy at a few locations. Here we use a transdimensional Bayesian inversion scheme, to better account for uncertainties and to understand the results of the inversions in the light of the highly non-linear and non-unique inverse problem.

2 DATA

We use continuous vertical-component data from the AlpArray seismic array, which combines ∼600 permanent and temporary

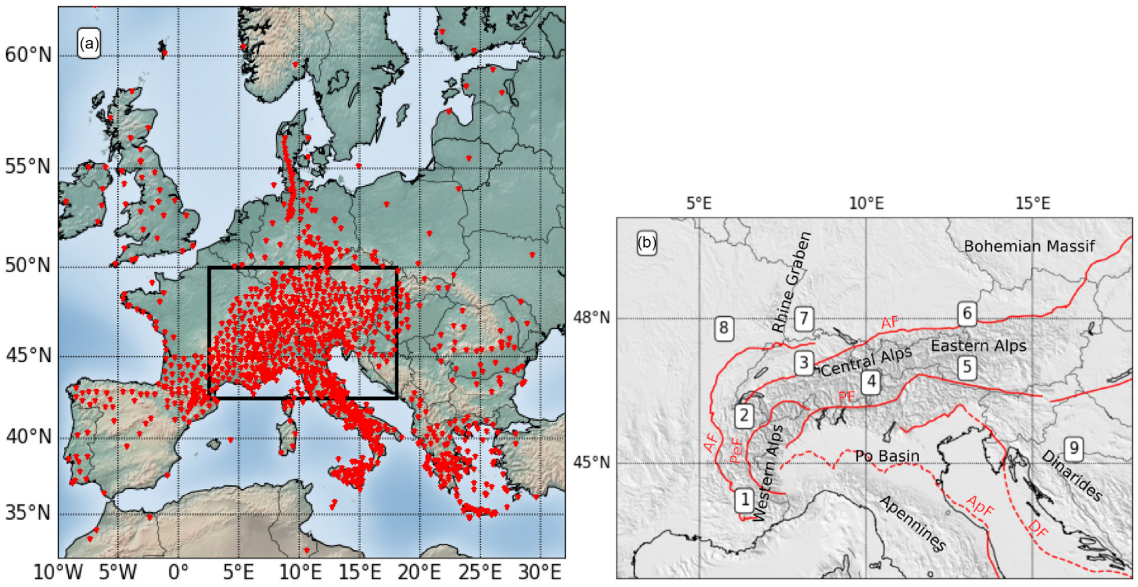

Figure 1. (a) Map of the seismic broad-band stations (red triangles) used in this study. Note that the subarrays that we use are located in the study area (black square), while all of the stations play the role of virtual sources depending on the location of each subarray (Section 3.1.2). (b) Simplified tectonic map of the study region, where red lines show the deformation fronts and the most important Neogene faults. Continuous lines show exposed structures, while dashed lines show structures hidden in the subsurface (simplified from Handy *et al.* 2010). AF: Alpine deformation front; ApF: Apennines deformation front; DF: Dinaric deformation front; PF: Periadriatic fault; PeF: Penninic front. The locations numbered 1–9 will be used later for the inversions.

broad-band stations that span the greater alpine area (Hetényi *et al.* 2018). The array provides a homogeneous coverage with station spacing of ∼50 km. With its homogeneous distribution and long residence time of temporary stations (typically 2–4 yr), the array is well suited for calculating seismic noise cross-correlations. We additionally use data from surrounding permanent stations, reaching a total of 1416 stations, covering a 3-yr period (2016–2018) of continuous data. The data are distributed by EIDA (European Integrated Data Archive), a service of ORFEUS (www.orfeus-eu.org). A complete list of the seismic networks used in this study is available in the data availability Section (A). Fig. 1 shows the station distribution as well as an overview of the tectonic setting.

Data preprocessing is identical to that of Soergel *et al.* (2020). After applying standard pre-processing (demean, detrend, downsampling to 1 Hz sampling rate, removal of instrument response), we use a 'comb filter' in order to reduce the contribution of earthquakes and high amplitude oceanic events: we filter the data in several frequency bands, normalize the signal in each band by its envelope and stack the normalized signals. This procedure ensures that the input signals to the cross-correlations are broad-band. For each station pair, we correlate the noise records using 4-hr windows. We then sum all 4-hr correlations to get the final correlation, following Poli *et al.* (2012). After selecting correlations within the distance range 30–3000 km, we obtain approximately 300 000 noise cross-correlations for further processing.

Fig. 2 shows a seismic section of all the cross-correlations binned into 1-km intervals, both without filtering, and in two different period intervals (3–30 s and 30–80 s). These sections have been oriented so that the causal part corresponds to waves propagating from the half-space 210–390° (30°) azimuth, that is the half-space in the direction of the North Atlantic Ocean which is the main source of seismic noise in the study area (Essen *et al.* 2003; Stehly *et al.* 2006; Kedar *et al.* 2008; Lu *et al.* 2021). Fig. 2 demonstrates that the cross-correlations have a clear Rayleigh wave arrival in a wide range of periods corresponding to the periods used by the comb filter. The

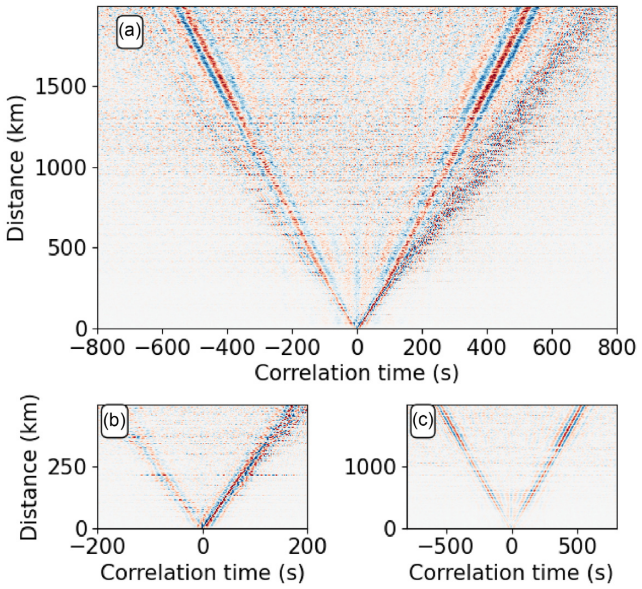

Figure 2. Seismic section of all cross-correlations, oriented so that the causal part corresponds to the sources located in the half space oriented in direction 300° azimuth (NNW–SSE), stacked in 1-km bins and normalized by their maximum amplitude. (a) Unfiltered correlations; (b) correlations filtered between 3 and 30 s (note the reduced distance range, for clarity) and (c) filtered between 30 and 80 s.

broad-band signature is also visible in the unfiltered sections, where the dispersion is clearly identified by the earlier arrival of the long-period waves as compared to the short-period waves. The greater variability of the short-period waves stems from strong lateral variations in propagation velocities, in particular velocity differences between waves propagating inside or outside sedimentary basins. The asymmetry of the correlations is significantly stronger at short

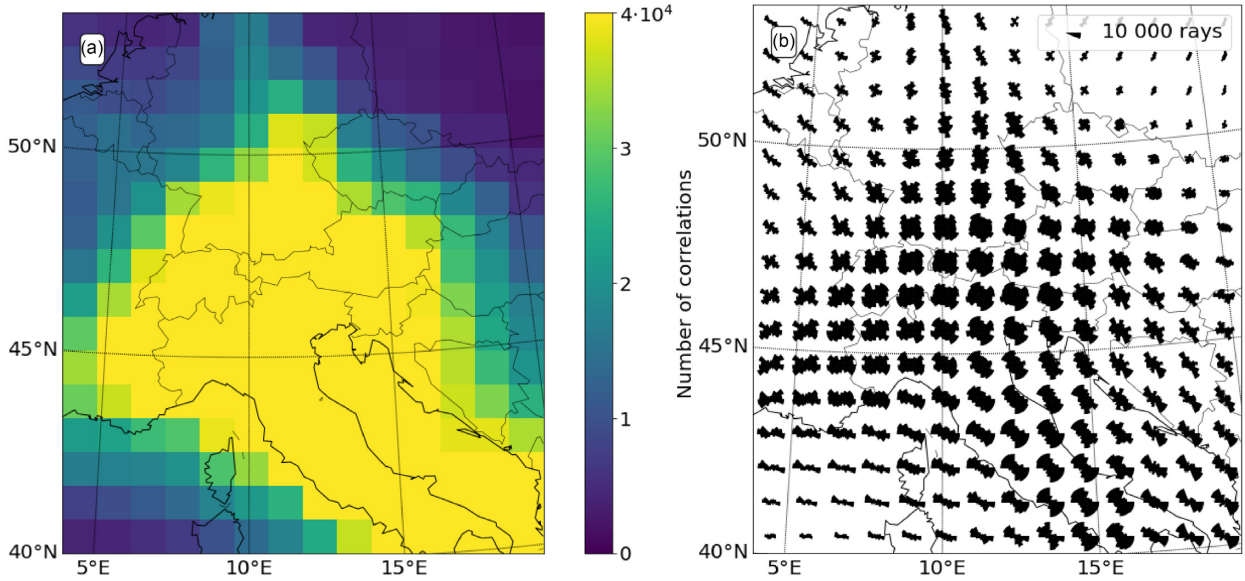

Figure 3. (a) Map of ray density (scale capped at 40 000) and (b) azimuthal coverage (scale capped at 10 000) for the cross-correlations used. Cells are approximately 85 km × 90 km, depending on latitude and longitude. The azimuthal coverage is given by the shapes in (b), in each area, the size of each wedge corresponds to the number of rays crossing the area with the corresponding azimuth. A perfectly even azimuthal distribution would show a circle, as all wedges would have the same size. The highest ray density is obtained in the central Alps, while the whole Alpine region has a good azimuthal coverage.

periods than at long periods, meaning that the distribution of noise sources covers a wider range of azimuths at long periods than at short periods. For all further processing we use the 'folded' correlation, that is the sum of the causal and the (flipped) anticausal part of the correlation, to ensure the best possible signal-to-noise ratio (SNR) over the complete range of possible azimuths. Fig. 3 shows that our study area is sampled by high ray density, typically significantly more than 40 000 rays in each cell, which are comparable in size to those used for the beamforming. Additionally, our station geometry shows that while the path orientation is somewhat skewed due to many stations in the Italian peninsula, all of the central part of the study area has very good azimuth sampling, and is substantially better than what can be obtained in Europe using teleseismic events (see fig. 2 in Paffrath *et al.* 2021).

3 METHODS

3.1 Beamforming

3.1.1 Principles and hypothesis

We use seismic noise cross-correlations to turn each station into a virtual source. We then use a beamforming analysis following Rost & Thomas (2002) to measure the fundamental mode Rayleigh-wave phase velocity between each virtual source and a given subarray of stations in the area of interest. Thus, we obtain for each subarray the Rayleigh-wave phase velocity as a function of the period and azimuth of the virtual source. Beamforming relies on the similarity of waveforms across the subarray, the only differences being due to time-shifts because of the different relative positions of the stations of the subarray with respect to the source. Given the correct phase velocity and propagation direction under the subarray, by shifting the waveforms accordingly, we obtain a constructive interference pattern. In the rest of this manuscript, we will call this method 'beamforming'.

Note that we use beamforming on the noise cross-correlations to retrieve the phase velocity under the subarray, not on the noise time-series to locate noise sources, as has been done previously (e.g. Stehly *et al.* 2006; Chevrot *et al.* 2007; Landès *et al.* 2010).

The hypothesis in beamforming is that the propagation velocity is constant beneath the subarray, that is the seismic structure is laterally homogeneous. The practical implication is that the subarray must be as small as possible, but yet sufficiently big so that the measurement error on the velocity for each virtual source is sufficiently small.

A second hypothesis is that the incoming wave front is a plane wave. To account for the relatively close proximity of the sources, in practice, we calculate delays for the shift of each trace based on the great-circle propagation time between the virtual source and each station of the subarray. To account for other azimuths (i.e. off great-circle propagation), we use propagation times for the virtual source, assuming it is shifted along a circle of constant radius as compared to the centroid of the subarray. While the great-circle deviations are generally significantly larger for teleseismic events than for the virtual sources used here, our analysis shows that they can still be significant for some locations and azimuths (see Section 3.1.3). In practice, it implies that we use circular wave fronts (on a sphere) with a significant curvature if the virtual source is close to the subarray, equivalent to the procedure used by Maupin (2011). For these short distances, the propagation path is very close to the great-circle. For longer distances between the virtual source and the subarray, the procedure leads to subplane wave fronts, and in practice corrects for great-circle deviations. In both cases it means that any small bias due to inhomogeneous seismic noise source distribution is corrected for.

A final hypothesis for beamforming, and for most other imaging methods aimed at quantifying azimuthal anisotropy, is that lateral heterogeneity of isotropic velocities does not bias the velocity variation with azimuth. For eikonal tomography, Ritzwoller *et al.* (2011) note that in some cases, the dependence of velocity with azimuth has a $\cos(\theta)$ component, θ being the azimuth. This dependence is

associated with the presence of strong velocity contrasts. For subarray measurements, Bodin & Maupin (2008) show that a lateral heterogeneity located close to an subarray can cause an apparent anisotropy, due to the deformation of the wave front and to wave diffraction on the heterogeneity. These effects are different for waves incoming through the heterogeneity or from the opposite side, and again result in a velocity variation with azimuth whose main component varies approximately with $\cos(\theta)$. It is therefore possible to distinguish these effects from the true azimuthal anisotropy which varies in $\cos(2\theta)$ and $\cos(4\theta)$. Depending on the size of the subarray, the characteristics of the heterogeneity and the wavelength, this effect may be more or less pronounced. However, if the $\cos(\theta)$ is very strong, it may somewhat bias the $\cos(2\theta)$ measurements (Ritzwoller *et al.* 2011). We will therefore use the amplitude of the $\cos(\theta)$ term as an indicator of this bias and exclude observation points where the $\cos(\theta)$ term is significant as compared to the $\cos(2\theta)$.

When using noise cross-correlation, one has to be aware of possible azimuthal biases related to a non-uniform noise sources distribution (Yao & van der Hilst 2009; Harmon *et al.* 2010). However, Harmon *et al.* (2010) show that for a station couple, the non-uniform distribution of noise sources translates into phase delays which depend mainly on azimuth of the station pair and much less on distance. For beamforming, we compare different signals within a subarray, for which distance and azimuth vary very little. We therefore expect this phase shift to be almost constant for the stations of the subarray, resulting in a systematic bias. As beamforming uses phase delays between stations, this systematic error cancels our when taking the difference of phase arrivals. In this way, we expect the effect of the non-uniform noise source distribution to be very small. A similar reasoning is also used for eikonal tomography (Lin *et al.* 2013; Kästle *et al.* 2021).

3.1.2 *Implementation*

For any given subarray, we exclude virtual sources less than 2.5 wavelengths from the centre of the subarray. This is standard for noise correlations, as smaller distances imply possible significant near-field terms and a risk of interference between the causal and anticausal parts of the correlations.

We seek to minimize the quantity

$$E(T, C, \theta) = \int_{t_0}^{t_0+\Delta t} \left(\sum_j s_j \left(T, t + \frac{\delta r_j}{C} \right) \right)^2 \mathrm{d}t, \quad (1)$$

where T is the chosen period, C is the phase velocity, θ is the azimuth, $[t_0, t_0 + \Delta t]$ is the time window used for the beamforming. s_j is the signal filtered around the period T and δr_j the distance difference between the centroid of the subarray and the virtual source on one hand and the station j and the virtual source on the other hand. The sum is performed over all the stations j in the subarray. When performing beamforming measurements, the sources are often supposed to be very far from the subarray in which case the wave fronts can be considered approximately plane. However, in our case, the virtual sources can be as close as 2.5 wavelengths from the subarray. We therefore follow Maupin (2011) and use circular wave fronts. Changing the azimuth in the beamforming procedure is equated to moving the virtual source along a circle centred on the centroid of the subarray.

We also define

$$\mathrm{d}(T, t, C, \theta) = \sum_j s_j \left(T, t + \frac{\delta r_j}{C} \right) \quad (2)$$

as the sum of the signals.

The data processing is as follows, for one virtual source i, a subarray and a given period T:

(i) Calculate the average group velocity between the virtual source and the subarray stations. The group velocity is for each station calculated by oversampling the signal and determining the time of the maximum of the signal envelope within a realistic velocity window (between 1 and 5 km s^{-1}).

(ii) Perform a grid search over phase velocity (C_i) and azimuth (θ_i) of the Rayleigh wave coming from the virtual source:

(a) For each station in the subarray, calculate the offset time between the station and the centre of the subarray for the selected Ci and θi.

(b) For each station, select a window centred on the arrival time of the Rayleigh wave at the subarray centre (calculated using the average group velocity) shifted from zero by the offset time value obtained in the previous step. For greater accuracy, the data are again oversampled.

(c) Normalize and stack the windows obtained in the previous step.

(d) Sum the square of the stacked signal. This gives an energy *Ei(Ci, θi)*.

(iii) Extract the phase velocity, the azimuth, the sum of the traces [*di(t, Ci, θi)*] normalized by the number of stations, as well as its maximum $d_{i,\max}$, corresponding to the maximum of the energy $E_{i,\max}$.

At the end of this process, we obtain an energy $E_{i,\max}$, a phase velocity $C_{i,\max}$ and an azimuth $\theta_{i,\max}$ as well as the optimal trace sum $d_i(t, C_{i,\max}, \theta_{i,\max})$ and its maximum $d_{i,\max}$, which represents the quality of the interference, 1 being constructive interference and 0 being destructive interference. We call the azimuthal deviation the difference $\theta_{i,\max} - \theta_r$ between the recovered azimuth of the plane wave and the azimuth of the virtual source.

For the phase velocities, we do a grid search using expected ranges: at less then 20 s period, we use the phase velocity interval 2.5–4.0 km s^{-1}, between 20 and 40 s 3.0–4.5 km s^{-1} and above 40 s we use 3.0–5.0 km s^{-1}, always with a step of 0.008 km s^{-1}. We tested this choice of parameters on a subset of data. The window length is set to three times the average signal period.

To obtain maps of anisotropy for a given period (Fig. 11), we define subarrays as follows: a subarray consists of stations located within an area delimited by two meridians and two parallels. We use the centroid of the subarray as the reference point for calculating the offsets. The minimum size is chosen so as to have the smallest possible size which allows for acceptable measurement errors and reducing the $\cos(\theta)$ term.

After extensive tests, this size was chosen as two wavelengths at 15, 30 and 40 s period, one wavelength at 50 and 60 s period and 1.5 wavelengths at 70 s period. At each period, the subarray has to meet two additional criteria, otherwise its dimension is increased until these criteria are met. First, the subarray has to have a minimum number of six stations. Secondly, there must be at least one station closer to each corner than to the centre of the subarray.

In order to obtain the distribution of anisotropy with depth, we require subarrays for which the station geometry is independent of period, and where good quality measurements are possible at fine period steps across a broad period range. For the locations at which we perform depth inversions, we use a fixed subarray size of 210 km (approximately one wavelength at 70 s period) and in period bands

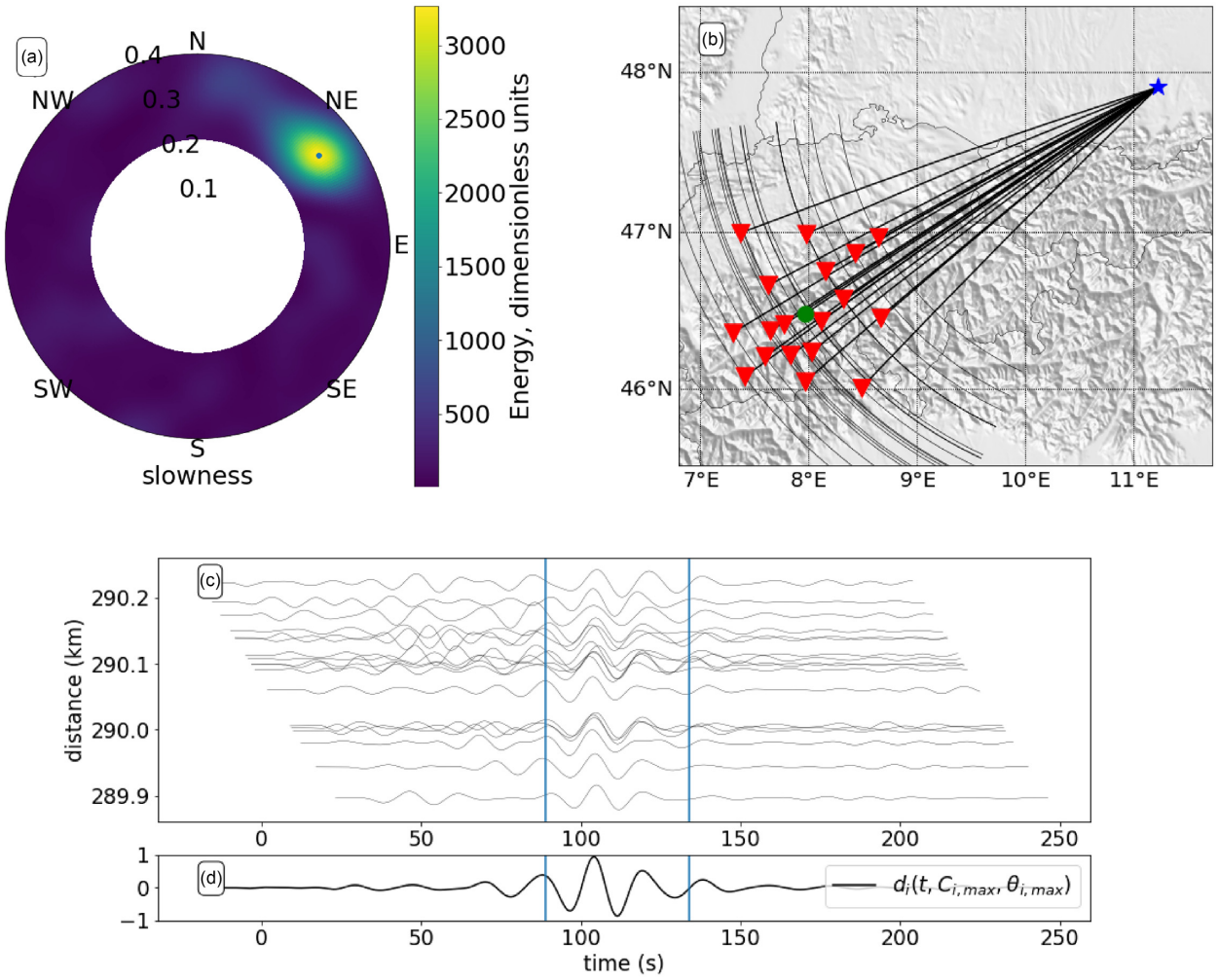

Figure 4. Example of beamforming result at 15 s period for a subarray in the central part of the study area. (a) $E(C_i, \theta_i)$ as a function of C_i (radius) and θ_i (angle). The location of the maximum value of the beam is indicated by a blue dot; (b) geometry of the virtual source (blue star), subarray stations (red triangles) and centroid (green dot). The bold black lines show the great-circle path between the virtual source and each station and the thin lines show the corresponding wave fronts; (c) the seismic section corresponding to the optimal phase velocity C_i and azimuth θ_i and (d) the corresponding stacked signal $d_i(t, C_{i,\max}, \theta_{i,\max})$. The blue bars correspond to the window used for the beamforming.

5 s wide from 10 to 75 s period. This provides us with dispersion curves with at best 12 points, in only a few locations.

3.1.3 Example of beamforming for one subarray

An example of phase velocity measurement following this algorithm is presented in Fig. 4, which presents an example of a beamforming result. In this example, we have chosen a very wide range of velocities and azimuths, which we will later restrict to $\pm 30^\circ$ from the azimuth of the source. The geometry of the stations within the subarray has an influence on the width of the optimal beam but it does not affect the position of the maximum amplitude (Löer *et al.* 2018). As we have a large number of virtual sources for each subarray, we will use the variability of the observations for a given azimuth to estimate uncertainties, rather than the width of the beam.

The beamforming yields a phase velocity C_i and azimuth θ_i for a given virtual source i, as well as an indication of the measurement quality ($d_{i,\max}$, the maximum of the normalized sum of waveforms). These intermediate results give important guidelines for the implementation of the method to estimate azimuthal anisotropy beneath the subarray.

The distribution of the measurement quality using all virtual sources for a subarray located in the central part of the study area is presented in Fig. 5(a). We observe that although there is no direct dependency of $d_{\max}$ with distance or azimuth, there are geographical variations. First, over a large part of Europe, $d_{\max}$ is close to 1.0, indicating that the waveforms used in the beamforming are similar, and that a constant velocity across the subarray is adequate to form the beam, thereby confirming that our hypotheses (see Section 3.1.1) are adequate for the analysis. In particular, examining beamforming across many subarrays, the quality of the measurement has no systematic dependency on the azimuth of the virtual source in relation to the subarray (with some specific exceptions, see below). This means that the uneven noise source distribution, with a strong dominance of noise sources in the North Atlantic Ocean, does not influence the beamforming in any significant way. We do however observe that the virtual sources located closest or furthest from the subarray sometimes have a lower $d_{\max}$ value, indicating that these virtual sources should have a lower weight in the anisotropy estimations. Secondly, virtual sources located in the Netherlands have a particularly low $d_{\max}$. This observation was recurrent for different subarrays so we consequently excluded these stations from further

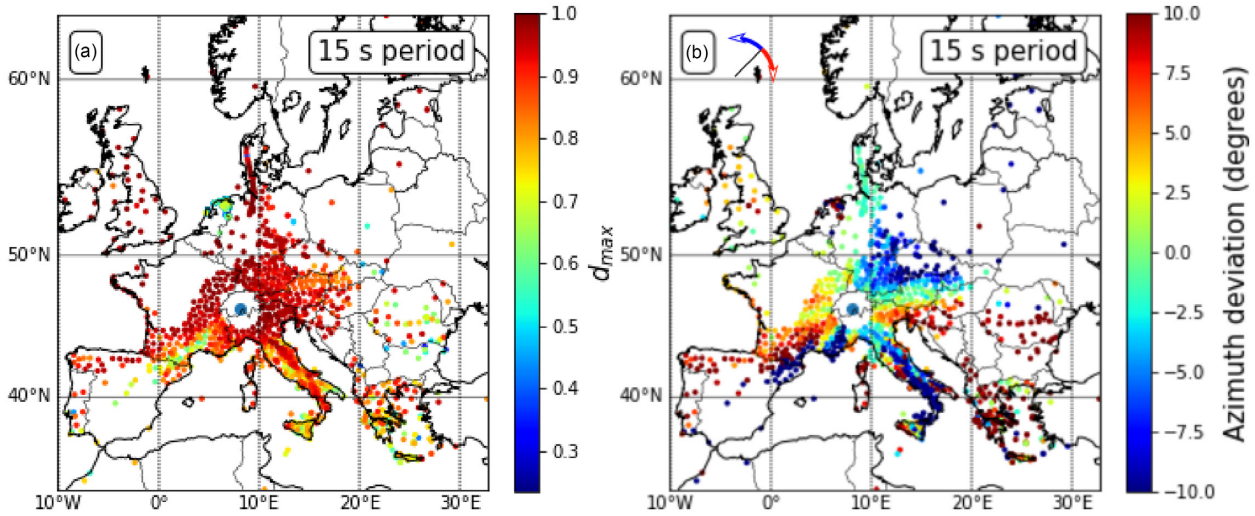

Figure 5. Example of results of the beamforming analysis at 15 s period for a subarray centred on the blue dot. All virtual sources located more than 2 wavelengths away from the centre of the subarray are plotted as coloured dots. (a) Quality of the measurements $d_{\max}$. (b) Azimuthal deviation (as defined in Section 3.1.2) of the Rayleigh wave propagating from the selected source to the subarray. Blue corresponds to an anticlockwise deviation, red to a clockwise deviation. The scale has been capped at $\pm 10^{\circ}$.

analysis. Finally, for this subarray some areas have lower values of $d_{\max}$, especially Italy, Greece and southern France. The location of areas with low $d_{\max}$ is dependent on period and subarray, so is related to propagation effects.

Fig. 5(b) shows the azimuth deviations for the same subarray and period. We observe that the deviation is strongly correlated with the azimuth of the virtual source. In particular, the azimuthal deviation is well observed northward north of the Alps and southward south of the Alps, with the exception of some Italian stations which have an azimuthal deviation towards the north. The deviations are explained by the presence of mountain ranges (the Alps and the Apennines in particular) which at 15 s period have lower Rayleigh-wave velocities (Lu *et al.* 2018a). That leads to ray paths circumventing them, causing the azimuthal deviations observed in Fig. 5. Our observations are coherent with those of Cotte *et al.* (2000), who attribute their observations of azimuth deviations at 30 s period for teleseismic events partly to large-scale propagation, partly to local ray bending due to the crustal structure. The areas corresponding to abrupt changes in azimuth correspond to the areas where $d_{\max}$ is low, as documented by Fig. 5(a). This means that the subarray and period dependent areas with low $d_{\max}$ can be explained by strong wave front distortions, thereby violating the underlying hypothesis for the beamforming. Overall, our results confirm that the use of $d_{\max}$ as a weighting factor for the anisotropy estimates (see Section 3.1.2) is meaningful.

3.2 Estimating Rayleigh wave anisotropy

Once measurements for each virtual source are obtained at a given period, we model the azimuthal variations of the Rayleigh wave phase velocities with both a π- and a 2π-periodic component:

$$C(\theta) = C_0 + A_1 \cos(\theta - \theta_1) + A_2 \cos(2(\theta - \theta_2)), \quad (3)$$

where θ is the azimuth (relative to the north, clockwise), and where coefficients C_0, A_1, A_2, θ_1 and θ_2 are obtained with a least-squares regression (Fig. 6). Note that theoretically, azimuthal variations of Rayleigh-wave velocities are not expected to show a 2π-periodicity (Smith & Dahlen 1973). Here the term $A_1 \cos(\theta - \theta_1)$ is included to accommodate for measurement biases due to lateral variations of isotropic shear wave velocities as detailed in Bodin & Maupin (2008). As shown by Ritzwoller *et al.* (2011), if this term (A_1) is significant (as compared to A_2), there may be significant measurement errors on the estimate of azimuthal anisotropy, including on the fast direction (θ_2).

Each observation $C_i(\theta)$ is treated as independent and weighted by the associated beam quality $d_{i,\max}$. To obtain a realistic estimate of the uncertainty of each estimated term (ΔC_0, ΔA_1, ΔA_2, $\Delta\theta_1$, $\Delta\theta_2$), we use a bootstrap approach where we construct a dataset of equal size by resampling the initial one with replacement and make a fit with this new data. Doing this a thousand times, we obtain a standard deviation on each estimated term which we use as an uncertainty estimate. This is equivalent to using the covariance matrix of the model parameters.

Three examples of anisotropy estimates at 15 s period are shown in Fig. 6. The first example (a) corresponds to a subarray in the Swiss Alps around 46.5°N, 8°E, where anisotropy is weak. Also, the values of A_1 and A_2 are similar. This means that the amplitude A_2 and the fast axis direction θ_2 for the terms in $\cos(2\theta)$ need to be interpreted with great care, or not considered. In the second example (b), located around 46°N, 10.5°E at the northern border of the Po plain, the value of A_2 is 10 times the value of A_1, indicating that both direction and amplitude of the azimuthal anisotropy can be interpreted with confidence. Similarly, example (c), located in the eastern Alps, shows a good fit using only $\cos(2\theta)$ terms.

3.3 Inverting Rayleigh wave anisotropy at depth

In the presence of weak elastic anisotropy, (Smith & Dahlen 1973) showed that, for a given period, azimuthal variations of Rayleigh wave phase velocities are π-periodic and given by:

$$C(\theta) = C_0 + C_1 \cos(2\theta) + C_2 \sin(2\theta). \quad (4)$$

Note that there is also a periodicity in $\pi/2$ [i.e. terms in $\cos(4\theta)$ and $\sin(4\theta)$] which we neglect here as their amplitude is much smaller than terms in $\cos(2\theta)$ for Rayleigh waves (Montagner & Nataf 1986; Montagner & Tanimoto 1991; Alvizuri & Tanimoto 2011; Maupin

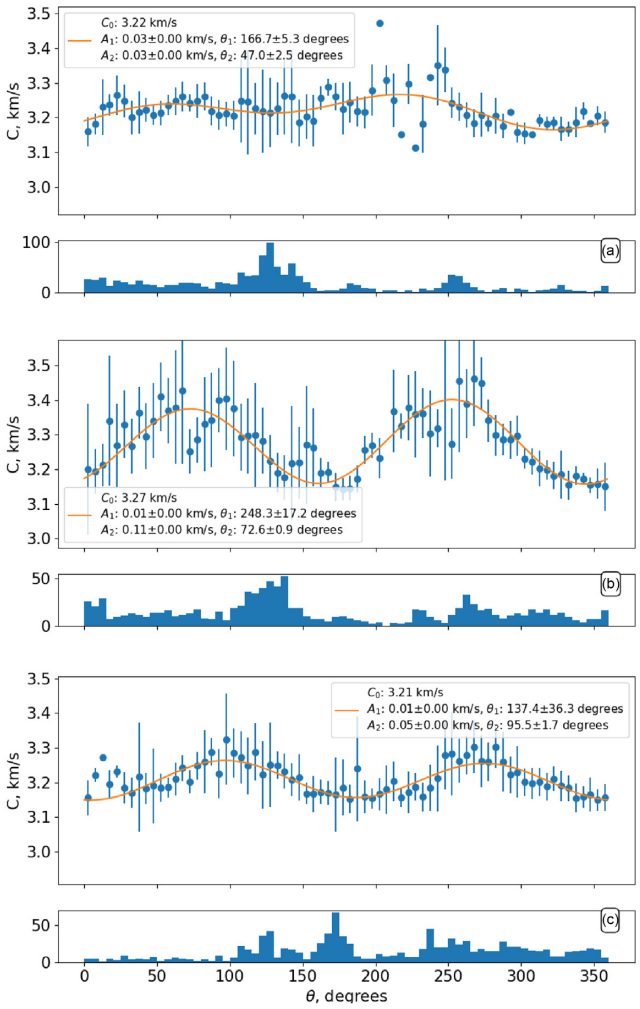

Figure 6. Examples of anisotropy measurement on three subarrays at 15-s period. The best fitting (eq. 3) model of velocity variations with azimuth, fitting each individual measurement weighted by its quality, is plotted in orange. Rather than showing all individual data points used in the calculation, the figure shows the mean velocity (filled blue circle) and standard deviation (blue bar) of all data points within 5° wide azimuth bins. The number of data points in each azimuth band is shown in the histogram at the bottom of each plot. The locations are shown on Fig. 15. They are located in the western Alps (a), the central Alps (b) and the eastern Alps (c).

& Park 2015). C_0 is the isotropic Rayleigh-wave phase velocity. Observations of C_1 and C_2 are given by the least-squares regression estimates carried-out in the previous step (see eq. 3):

$$\begin{aligned} C_1 &= A_2 \cos(2\theta_2) \\ C_2 &= A_2 \sin(2\theta_2). \end{aligned} \tag{5}$$

Note that the 2π-periodic terms observed in the previous steps (A_1 and θ_1) are not used in the inversion. This part of the anisotropic signal results from bias in the array measurement of phase velocities due to wave front distortion by 3-D heterogeneities (Bodin & Maupin 2008). The associated uncertainties on C_1 and C_2 can be estimated from the uncertainties ΔA_2 and $\Delta\theta_2$ (see Section 3.2), by differentiating eq. (3):

$$\begin{aligned} \Delta C_1 &= \sqrt{(\Delta A_2 \cos(2\theta_2))^2 + (2A_2\Delta\theta_2 \sin(2\theta_2))^2} \\ \Delta C_2 &= \sqrt{(\Delta A_2 \sin(2\theta_2))^2 + (2A_2\Delta\theta_2 \cos(2\theta_2))^2}. \end{aligned} \tag{6}$$

The observed values of C_1 and C_2 at each period (associated to their uncertainties ΔC_1 and ΔC_2) can then be inverted at depth. Here we use a transdimensional Bayesian inversion scheme adapted from Bodin *et al.* (2016). The unknown 1-D anisotropic profile at depth is parametrized in terms of a stack of layers with constant seismic velocities, between 0 and 100 km depth. In the transdimensional formalism, the number of unknowns is variable. The number of layers and the thickness of each layer is variable. Furthermore, each layer in the inversion can be either isotropic and described solely by its isotropic shear-wave velocity, or azimuthally anisotropic and described by three parameters: (1) the isotropic shear-wave velocity; (2) the peak to peak level of azimuthal anisotropy and (3) the direction of the horizontal fast axis relative to the north (Romanowicz & Yuan 2011). The layer thickness is also variable and the last layer is an isotropic half-space. This inversion scheme uses a piecewise constant parametrization for anisotropy model parameters. This choice in parametrization leads to slightly 'blocky' outputs, especially as the inversion scheme favourizes models with fewer anisotropic layers. The influence of the parametrization for transdimensional Bayesian inversions has been studied by Hawkins *et al.* (2019).

Since we are interested in the distribution of anisotropy at depth, only the anisotropic part of the dispersion curves C_1 and C_2 are inverted and shown here, not C_0. Practically we chose to use C_0 values and an earth model compatible to those values, and during the inversion we allowed only small variations of the isotropic earth model. We used the dispersion curves and model from Lu *et al.* (2018b) while using a narrow prior distribution for the model, which is only allowed to deviate up to 5 per cent. For anisotropic parameters, we use wide and uninformative prior distributions: the peak to peak amplitude of anisotropy can vary from 0 to 30 per cent and the direction from 0° to 180°. Thirty per cent may seem unrealistic, but the aim is to give as much freedom to the inversion for it to be completely data driven. Fig. 7 shows that the choice of isotropic model has a negligible influence on the anisotropic sensitivity kernels, so the anisotropic inversions are not biased by errors in the isotropic earth model.

For the forward modelling of $C_1(T)$ and $C_2(T)$, we use the kernels from Bodin *et al.* (2016) after Maupin (1985) and Montagner & Nataf (1986). We suppose our medium is composed of a stack of layers with each isotropic velocities V_s and V_p, peak to peak level of anisotropy $\frac{\delta V_s}{V_s}$ and $\frac{\delta V_p}{V_p}$ and an anisotropy fast direction ψ_2. We suppose that *P*-wave phase velocity and anisotropy is proportional to *S*-wave velocity and anisotropy respectively, with $\frac{V_p}{V_s} = \frac{\delta V_p}{\delta V_s} = 1.73$ (Obrebski *et al.* 2010), and we therefore only invert for V_s, δV_s and ψ_2. Each layer is thus a horizontal transverse isotropic medium, with full elastic tensor:

$$\mathbf{C}_{mn} = \begin{pmatrix} A & A-2L & A-2N & 0 & 0 & 0 \\ A-2L & C & A-2L & 0 & 0 & 0 \\ A-2N & A-2L & A & 0 & 0 & 0 \\ 0 & 0 & 0 & L & 0 & 0 \\ 0 & 0 & 0 & 0 & N & 0 \\ 0 & 0 & 0 & 0 & 0 & L \end{pmatrix}$$

with $C = \rho(V_p + \frac{\delta V_p}{2})^2$, $A = \rho(V_p - \frac{\delta V_p}{2})^2$, $L = \rho(V_s + \frac{\delta V_s}{2})^2$ and $N = \rho(V_s - \frac{\delta V_s}{2})^2$, where axis 3 is vertical and axis 2 is in the ψ_2 direction. The phase velocities for Rayleigh and Love waves can be computed and for weak anisotropy, the values for C_1 and C_2 are:

$$C_1(T) = \int_{z=0}^{\infty} \left(\frac{\partial C_1(T)}{\partial A_0(z)} B_c(z) + \frac{\partial C_1(T)}{\partial L_0(z)} G_c(z) \right) \mathrm{d}z$$

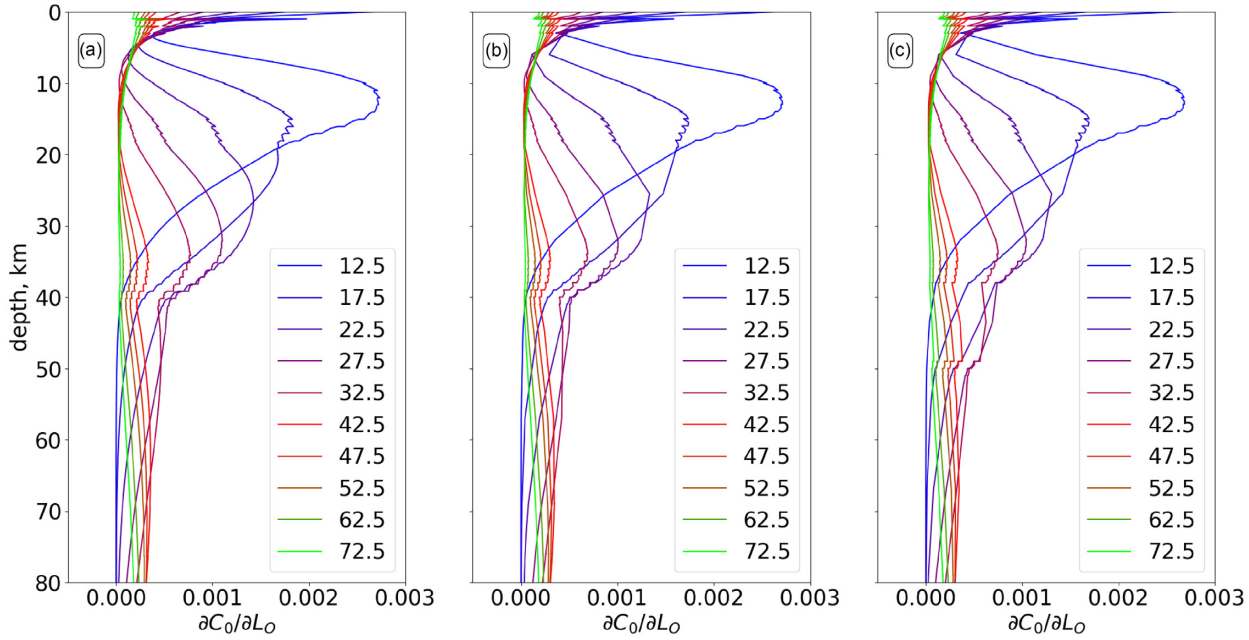

Figure 7. Curves of $\frac{\partial C_1(T)}{\partial L_0(z)}$ with depth for three different V_s models. This kernel depicts how the the anisotropy in Rayleigh wave phase velocities at a given period depends on the anisotropy at depth. In (a) for the average model from Fig. 8, in (b) for the reference model from Lu *et al.* (2018b) and in (c) for the reference model with a Moho 10 km deeper.

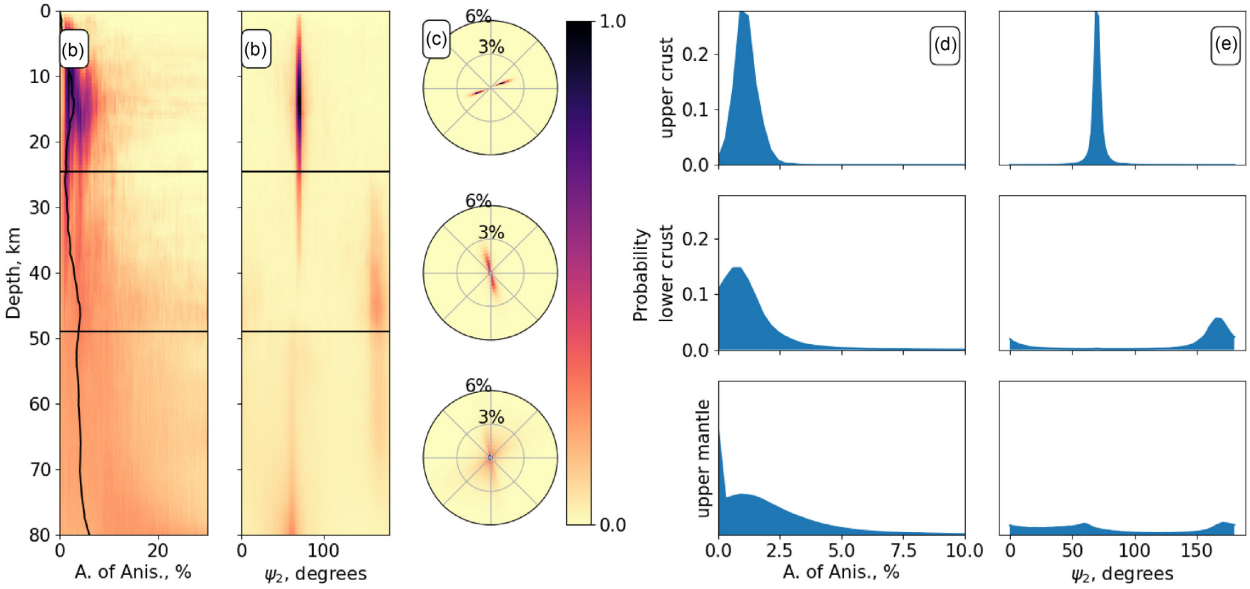

Figure 8. Depth inversion results for a subarray located around 46.5°N, 10°E (location 4 of Fig. 14). The solution is a large ensemble of models with different parametrizations (different number of isotropic and anisotropic layers). (a) Probability distribution of the amplitude. (b) Probability distribution of the direction of the fast axis of anisotropy. The black line in (a) shows the average amplitude and the horizontal black lines in (a) and (b) indicate the limits of the three layers over which we integrate anisotropy. (c) Density plot of anisotropy parameters integrated over the three different depth ranges. The radius in the polar plots indicate amplitude and the angle gives direction of the fast axis of anisotropy. The colour scale indicates the normalized probability of a given combination of amplitude and fast direction. Panels (d) and (e) show the marginal distributions of δV_s (d) and of ψ_2 (e) for each of the three depth ranges. The vertical scale is chosen such that the surface of the blue area is 1, that is the fraction of models with a given amplitude or (ψ_2) range corresponds to the blue area within that range.

$$C_2(T) = \int_{z=0}^{\infty} \left(\frac{\partial C_2(T)}{\partial A_0(z)} B_s(z) + \frac{\partial C_2(T)}{\partial L_0(z)} G_s(z) \right) \mathrm{d}z$$

with $B_c = \frac{C-A}{2}\cos(2\psi_2)$, $B_s = \frac{C-A}{2}\sin(2\psi_2)$, $G_c = \frac{L-N}{2}\cos(2\psi_2)$, $G_s = \frac{L-N}{2}\sin(2\psi_2)$, $A_0 = \frac{5}{8}A + \frac{3}{8}C$ and $L_0 = \frac{L+N}{2}$. For any further details, we refer to appendix A of Bodin *et al.* (2016) and references therein. We show examples of kernels for C_1 in Fig. 7. It is important to keep in mind that for this kind of fully non-linear inversions, we are calculating kernels for every model proposed in the course of the inversion, however as can be seen in Fig. 7 the kernels do not change significantly for different isotropic velocity models. Therefore,

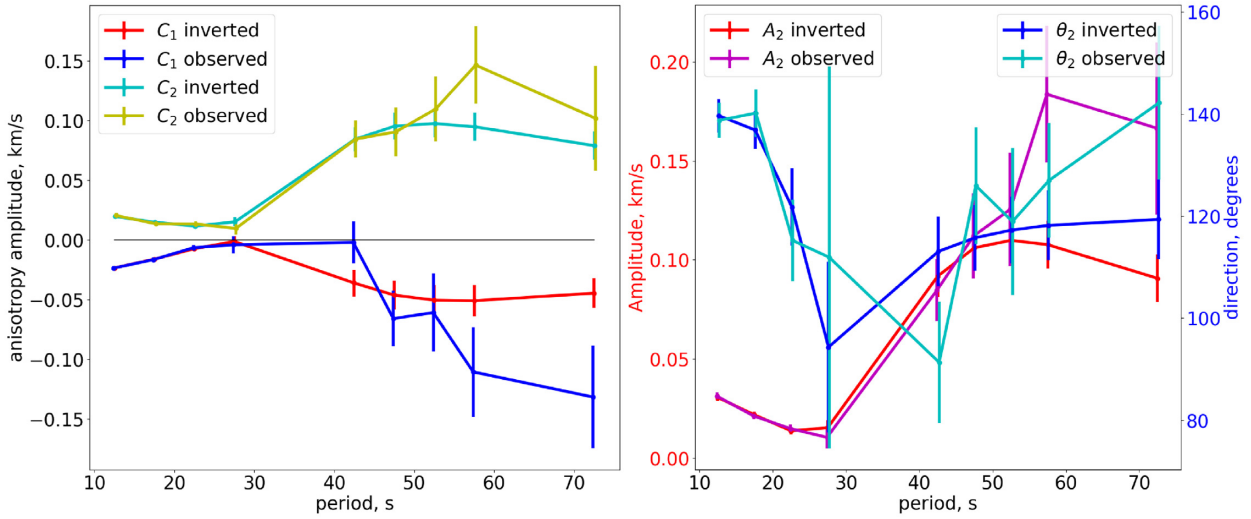

Figure 9. Dispersion curves for the inversion in Fig. 8, that is for a subarray located around 46.5°N, 10°E (location 4 in Fig. 1) with the associated uncertainties. Observed data and associated uncertainties are shown in blue and yellow. On the left, the fit for C_1 (observed data in blue, inversion result in red) and C_2 (observed data in yellow, inversion result in cyan). On the right, the fit for A_2 (left scale, shades of red) and θ_2 (right scale, shades of blue). All the different sampled models in the ensemble solution provide different dispersion curves. The data fit is better at shorter periods as the inversion adapts to the smaller data uncertainties in this period range. The dispersion curves for all other locations are shown in Figs S8 and S9.

errors on the isotropic model will not project into the anisotropic inversion.

In a Bayesian framework, the solution is not a single model providing optimal data fit, but a large ensemble of models with different parametrizations approximating the posterior distribution, that is the probability of the model, given the observed data (Smith *et al.* 1991; Box & Tiao 1992; Gelman *et al.* 1995). The ensemble of models is explored with a Monte Carlo method based on the reversible jump algorithm (Green 1995). For details about the implementation of the inversion, we refer the reader to Bodin *et al.* (2012, 2016), and Yuan & Bodin (2018).

The outcome of Bayesian inversions is commonly underexploited, with the results often being presented solely through average values and standard deviations. It is on the contrary fruitful to explore the wealth of information contained in the ensemble solution through different angles of analysis and visualization, each one giving additional insight to precise geophysical questions. In Fig. 8, we present an example of inversion for a subarray at 46.5°E, 10°N (location 4 in Fig. 1). The distribution of sampled models describes the posterior solution and can be visualized in different manners. In Figs 8(a) and (b), the ensemble solution is projected onto a grid, and presented as a density plot (i.e. a histogram), where each point of the grid is coloured according to the number of models that cross it. This allows us to show, at each depth, the probability of a given amplitude range and direction range for shear-wave anisotropy. Note that individual 1-D models have a variable number of isotropic and anisotropic layers. This way of displaying the probabilistic solution does not show whether individual models contain thin isotropic layers, thin layers with strong anisotropy, or thick layers with small anisotropy, nor to easily identify the correlations and trade-offs between anisotropy amplitude and direction.

To extract some key features from this complex probabilistic solution, we display the posterior distribution for anisotropy integrated over a given depth range as defined by Romanowicz & Yuan (2011) (Fig. 8c). Here we propose to reduce the parameter set by integrating over specific depth ranges that have a meaningful sense (upper crust, lower crust, uppermost mantle), and plot the probability density of each of the obtained parameters. We show the amplitude and direction of the anisotropy integrated over three layers for each model: upper crust, lower crust and uppermost mantle down to 80 km depth. The Moho is defined as the depth at which the isotropic shear wave velocity reaches 4.1 km s^{-1} in the model of Lu *et al.* (2018b) and we set the upper/lower crust limit as half the Moho depth. This choice is justified by the rheological difference between upper and lower crust (brittle upper crust and ductile lower crust) and the chemical difference between crust and mantle lithosphere. This type of visualization is complementary to the plots in Figs 8(a) and (b), in particular because it becomes possible to see the correlations between fast direction and amplitude of anisotropy in each investigated depth interval. Other ways of projecting the posterior could be explored, such as for example plotting the distribution of interfaces between layers with depth. Isotropic layers are not shown on Figs 8(a) and (b), as the fast direction in an isotropic layer is not defined. Isotropic layers can dominate at a given depth and they are shown on Figs 8(c), (d) and (e). Isotropic layers decrease the average of A_2. Additionally, integrating anisotropy over several layers with different fast directions can lead to anisotropy amplitudes smaller than expected. This explains the differences between the histograms in Fig. 8(d) and the density plots in Fig. 8(a).

To illustrate the advantage of the depth integration, consider the density plots of ψ_2 (Fig. 8b). They show three apparent layers that overlap partially: one between 0 and 40 km depth at ∼70° azimuth, one between 30 and 70 km depth at ∼180° and one between 50 and 80 km depth at ∼70°. Once the integration over each of the 3 depth ranges is carried out, the fast directions in upper and lower crust are clearly separated, however, the choice of the limits between the depth ranges does not exactly fit the apparent limit between the layers as observed in Fig. 8b). We also observe that the integrated amplitude and direction of anisotropy in the uppermost mantle are poorly resolved (Fig. 8c).

Fig. 9 shows the comparison between predicted and observed data. We observe that the data fit is better at short periods as

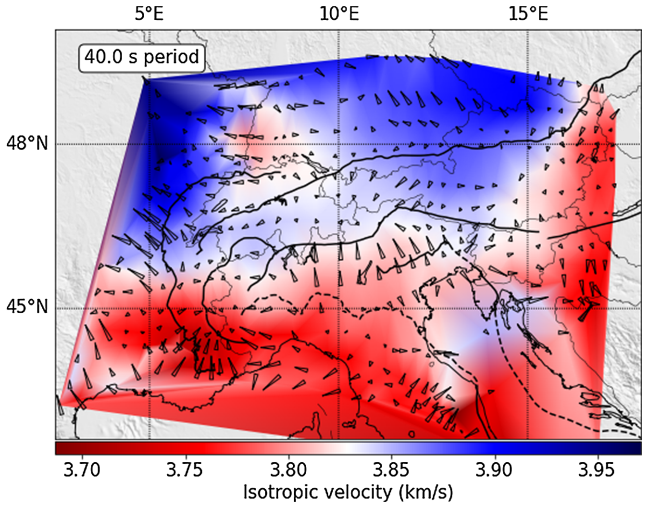

Figure 10. Map of the cos(θ) component at 40 s period superimposed on the map of C_0 at the same period, smoothed over the study area. The thin part of the wedges points in the faster direction. The θ_1 component generally points towards higher phase velocities, but not always.

compared to long periods, because the latter are associated with larger uncertainties, thus carrying less weight in the inversions.

4 RESULTS

We first present results for Rayleigh wave anisotropy at different periods as estimated by beamforming. Note that for these maps, the size of the subarrays (hence the lateral resolution) varies with period. In a second part, we present variations of shear-wave azimuthal anisotropy with depth. Those inversion results are only shown at a few locations where the station geometry and data quality was such that reliable observations could be obtained across subarrays of identical size across a broad period range.

4.1 2-D maps of Rayleigh-wave phase velocity anisotropy

Azimuthal anisotropy was measured using all available sources and subarrays covering the whole Alpine area in the period bands 10–20 s, 25–35 s, 35–45 s, 45–55 s, 55–65 s and 65–75 s. The subarray sizes adapt to the distribution of stations, with a minimum size that depends on the subarray: 100 km for the 10–20 s period band, four times the wavelength (assuming a velocity of 3 km s^{-1}) for the 25–35 s and 35–45 s period bands, twice the wavelength for the 45–55 s, 55–65 s period bands and three times the wavelength for the 65–75 s period band. Note that the choice of size depends on SNR in a given frequency range, which is why we could reduce the array size in the mid-period ranges. Because of the increasing size of the subarrays, we have fewer subarrays at longer periods.

Fig. 10 shows the map of the θ_1 anisotropy at 40 s [terms in cos(θ)] superimposed over the map of C_0 at 40 s period. Following Ritzwoller *et al.* (2011), we interpret the anisotropy in cos(θ) as being the effect of lateral heterogeneities. Such effects can create biases on estimates of A_2 and θ_2 (Bodin & Maupin 2008; Ritzwoller *et al.* 2011). Likewise, Mauerberger *et al.* (2021) explain anomalous cos(θ) anisotropy in Scandinavia as linked to topography of the lithosphere-asthenosphere boundary. In our case, the cos(θ) term has high amplitude and spatial coherence at 40 s period. Fig. 10 shows that strong θ_1 anisotropy is correlated with C_0 gradients and generally points towards higher C_0, but not always as can be seen in the southwest tip of the Alps. At shorter period, there is little spatial coherency to the cos(θ) terms

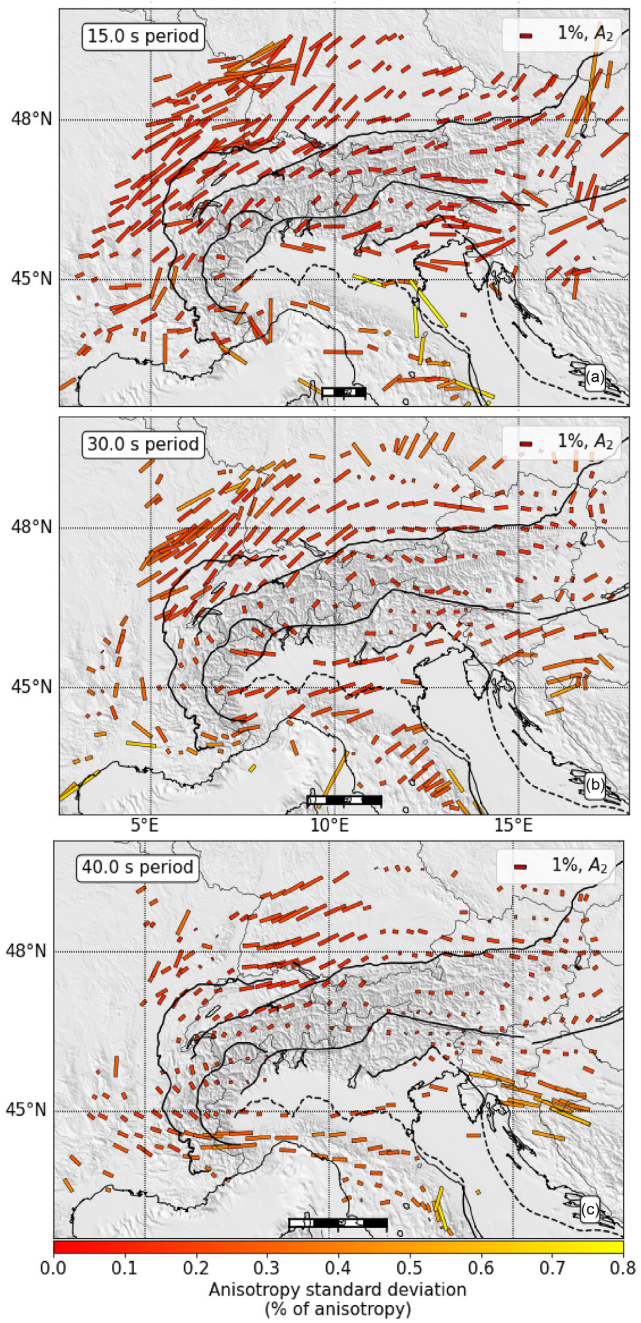

Figure 11. Maps of Rayleigh-wave azimuthal anisotropy at 15 (a), 30 (b) and 40 s (c) period. For each subarray, the coloured bar indicates the cos(2θ) component. Each bar is located at the centroid of the corresponding subarray. The length of the bar corresponds to the value of A_2 (expressed as a percentage of the isotropic velocity C_0) and its direction to the value of θ_2. The colour indicates the uncertainty on A_2, red being small uncertainty and yellow large uncertainty. The black-and-white bar in the bottom part of each map shows the median size of the subarrays. The subarrays are initially chosen so that they are uniformly distributed over the area, but the inhomogeneous distribution of stations (especially at the edge of the network) results in a non-uniform distribution of the centroids and larger subarray sizes at the edges.

Fig. 11 shows maps of the θ_2 anisotropy [terms in cos(2θ)] at different periods. To filter out measurements biased by strong

heterogeneities, we do not show the $\cos(2\theta)$ anisotropy at locations where A_1 is greater than 70 per cent of A_2. In addition, unstable measurements (where the standard deviation of A_2 is greater than 20 per cent of A_2) as well as outliers (where A_2 is greater than 200 m s^{-1}) are also rejected. However, all points with insignificant anisotropy (A_2 less than 1 per cent of the isotropic phase velocity C_0) are shown, as information of small or absent anisotropy would otherwise be lost.

The number of reliable measurements depends on the chosen period band, with a particularly high number at 15 and 30 s period and a lower number at longer periods. Uncertainties on anisotropy amplitude are smaller than 0.3 per cent of the isotropic velocity, much less than the anisotropy, and uncertainties on the direction (which can be seen in Fig. S1) are less than 10°, except when the anisotropy amplitude is low (less than 0.5 per cent). We only show maps up to 40 s period, as there are very few reliable anisotropy estimates at longer periods.

As expected, the lateral variations of anisotropy get smoother with increasing period, as wavelength and subarray size increase with period. At short periods (15 and 30 s), fast directions are roughly parallel to the strike of the Alps, with smaller amplitudes in the Alps themselves, although fewer measurements were possible there due to stronger heterogeneity. A strong NE-oriented fast axis of anisotropy is also observed northwest of the Alps. At 30 s period in the Apennines, and contrary to what is observed in the Alps, fast directions are perpendicular to the mountain range.

4.2 Depth inversions

A depth inversion is required to fully interpret the variation of anisotropic parameters with period in terms of depth variations of shear wave anisotropy. However, our tests show that the dispersion obtained from the beamforming as performed in Section 4.1 does not provide enough measurements to perform a depth inversion accurately. We therefore measure phase velocity on narrower period bands (5 s wide instead of 10 s) to obtain more phase velocity measurements, which requires us to make new beamforming measurements. Given the size of the dataset and the lack of coverage at long periods, we cannot perform a depth inversion at each geographical location. We therefore only analyse a limited number of locations, where we could define constant size subarrays across a broad period range, with well resolved estimates of A_2 and θ_2. The beamforming analysis was therefore carried out specifically for nine locations, independently of the results shown in Fig. 11. Given these limitations, we chose five areas in the Alps, one in the Dinarides and three north of the Alps (locations shown in Fig. 1). We could not perform a depth inversion in the Apennines, due to lack of long period data.

The depth inversions for four illustrative locations are shown in Fig. 12, with the corresponding marginal distributions shown in Fig. 13. The first location (location 1 in Fig. 1) shows an example of inversion results with only few measurements, that is only five periods with reliable estimates of A_2 and θ_2. Results are shown in Figs 12(a) and 13(a). Insufficient data leads to high uncertainties, which is especially visible on the density plot of δV_s. However, when integrating anisotropy over the three different depth ranges, the spread is less prominent, as we effectively reduce the parameter space and thus reduce the uncertainty on each parameter. The amplitude and direction of anisotropy are much better resolved in the upper crust and the uppermost mantle than in the lower crust.

Figs 12(b) and 13(b) correspond to location 5, in the eastern Alps. This location is representative of other locations in the Alps (locations 2, 3 and to a lesser extent 4), with a thick layer with fast directions oriented N60° to N90° over a layer with fast directions oriented N160° to N180° in the uppermost mantle. The transitions between these layers do not occur at the defined boundaries (upper-lower crust, Moho), which explains the broad spread in fast direction after integration over each of the three layers, especially in the lower crust.

Figs 12(c) and 13(c) correspond to location 8, which is representative of the region north of the Alps (locations 6, 7 and 8). It has a thin but strongly anisotropic layer in the lower crust with fast directions between N30° and N90° and a characteristic spike in the amplitude profile, while the uppermost mantle has a comparatively low anisotropy amplitude. The fast direction also varies much less with depth than at the other locations.

Figs 12(d) and 13(d) correspond to location 9 in the Dinarides. As for location 1, the inversion uses fewer points than elsewhere, and lacks measurements at periods longer than 50 s. However, it shows four layers, more than at any other location, with very sharp changes in direction, for example between the upper and lower crust, with overall poorly constrained anisotropy amplitudes. All density profiles are shown in Figs S2, S3 and S4 and all corresponding marginal distributions in Figs S5, S6 and S7. It is particularly apparent in Fig. 12(d) that transitions in anisotropy fast directions can appear as abrupt, but such seemingly abrupt changes are always correlated with a lower amplitude of the anisotropy. These transitions are due to the choice of piecewise constant parametrization, which enhances the visual impression of a block like structure.

Fig. 14 shows a map of the integrated anisotropy for each of the three layers at each of the nine locations. It is important to keep in mind that depth ranges are defined from Moho depths, and are therefore different for each location. The size of the density subplots corresponds approximately to the size of the subarrays.

We acknowledge here that the probabilistic ensemble solution produced at each location is complex and difficult to interpret. The solution is made of different models with different parametrizations, that is different number of anisotropic and isotropic layers. The only way to interpret this complex distribution is to project it on a simpler parameter space, and to calculate marginal distributions on a number of relevant parameters (anisotropy at the given depth, integrated anisotropy within a given depth range). To help the reader with the interpretation of the probabilistic solution, we show in Table 1 the average and standard deviation for the distribution of integrated anisotropy at different depth ranges, as well as Moho depth and the probability that the depth range is entirely isotropic. Due to the presence of isotropic layers in individual layered models, the integrated amplitude of anisotropy over a depth range is lower than what is visually apparent in the 2-D density plots.

A first result of the inversions is that for the upper crust, fast directions are overall parallel to the Alps, with the exception of the SW extremity of the Alps (location 1). The lower crust depicts fast directions that are different from those of the upper crust beneath several locations (locations 2, 4, 7 and 9). Results at location 9 are fundamentally different from the other locations, with strong anisotropy in each of the three layers, each with a distinct fast direction.

In the lower half of the alpine crust (locations 2, 3, 4 and 5) we observe fast directions oriented parallel to the mountain chain (with the exception of location 4, where the fast direction in the lower crust is oriented north–south), whereas in the mantle, the fast axis of anisotropy is oriented north–south. At the southwestern tip of

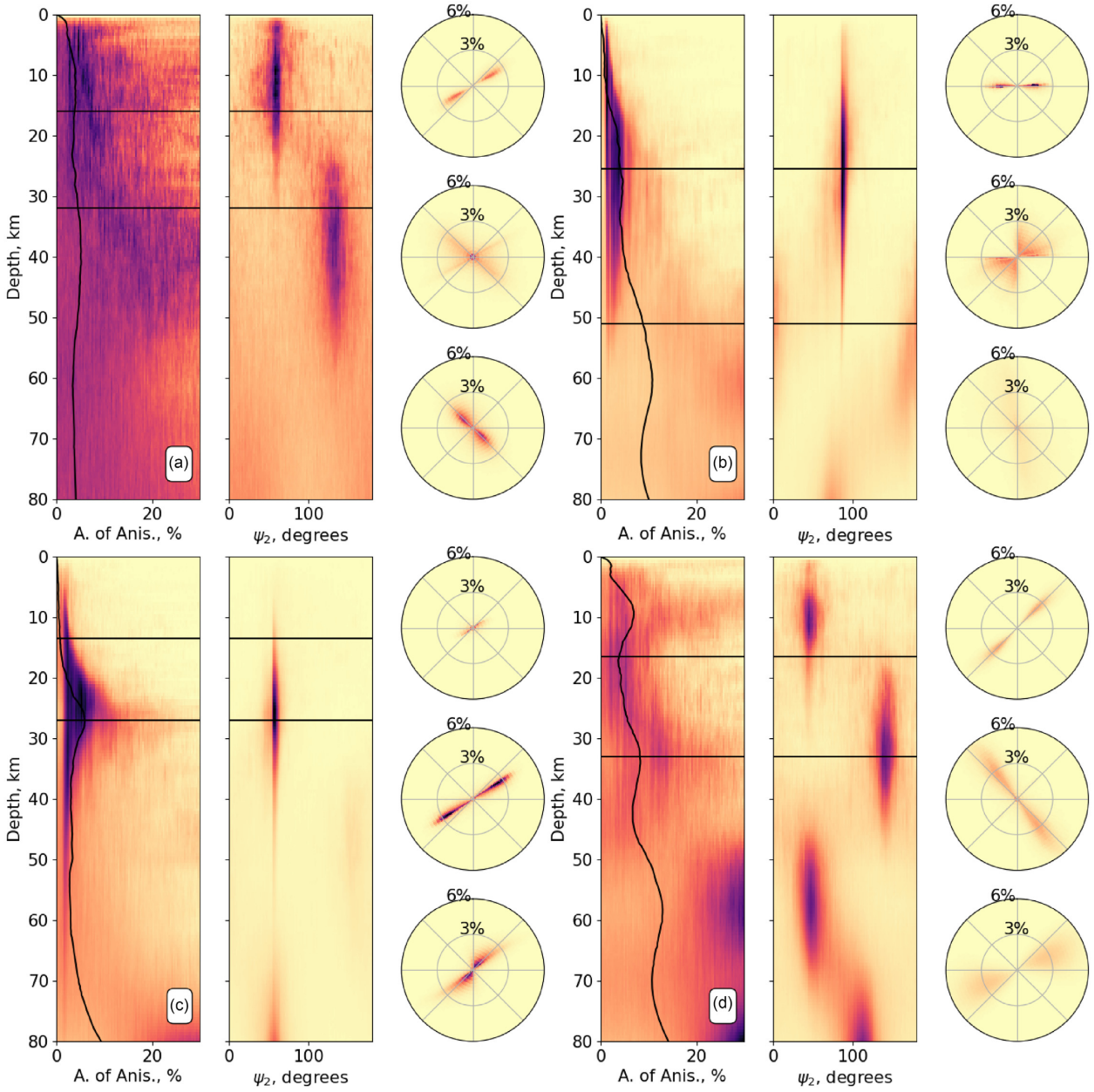

Figure 12. Noteworthy depth profiles corresponding to locations 1, 5, 8 and 9, figure layout similar to Fig. 8. The profile of location 1 (a) is the profile with the least data (only five measurements). Location 5 (b) shows an example of a profile in the Alps. Location 8 (c) shows a typical profile of the data north of the Alps. Location 9 (d) shows the only profile in the Dinarides. The colourscale is the same as in Fig. 8. The map of the locations is shown in Fig. 1.

the Alps (location 1) we observe fast directions oriented east–west, perpendicular to the Alps, in the lower half of the crust (but with high uncertainties), while in the uppermost mantle fast directions are oriented NW–SE, parallel to the belt. North of the Alps (locations 6 and 7) the fast axis of anisotropy in the lower half of the crust is oriented 25°N in the west (location 7) but 75°N in the east (location 6) with similar directions in the uppermost mantle: 60°N in the west and 40°N in the east (albeit with high uncertainties).

In the uppermost mantle, on the other hand, fast axis directions beneath the Alps are oriented in north–south direction (with the exception of location 1, which has a fast axis oriented NW–SE), as opposed to the three locations north of the Alps (locations 6, 7 and 8) which have an anisotropy similar to what is observed in the crust. At location 4, in the central Alps, the fast axis direction is not well constrained and shows a low amplitude.

Northwest of the Alps, location 8 shows a strong anisotropy parallel to the Alpine arc which is already observed on the maps by period, at all depths.

In the Dinarides (location 9), the upper and lower half of the crust behave very differently, with the fast axis in the upper crust having a SW–NE orientation whereas the fast axis in the lower crust has a SE–NW orientation and the fast axis in the mantle is oriented east–west. However, for this particular location we do not have data at periods longer than 50 s, the mantle is thus less well constrained.

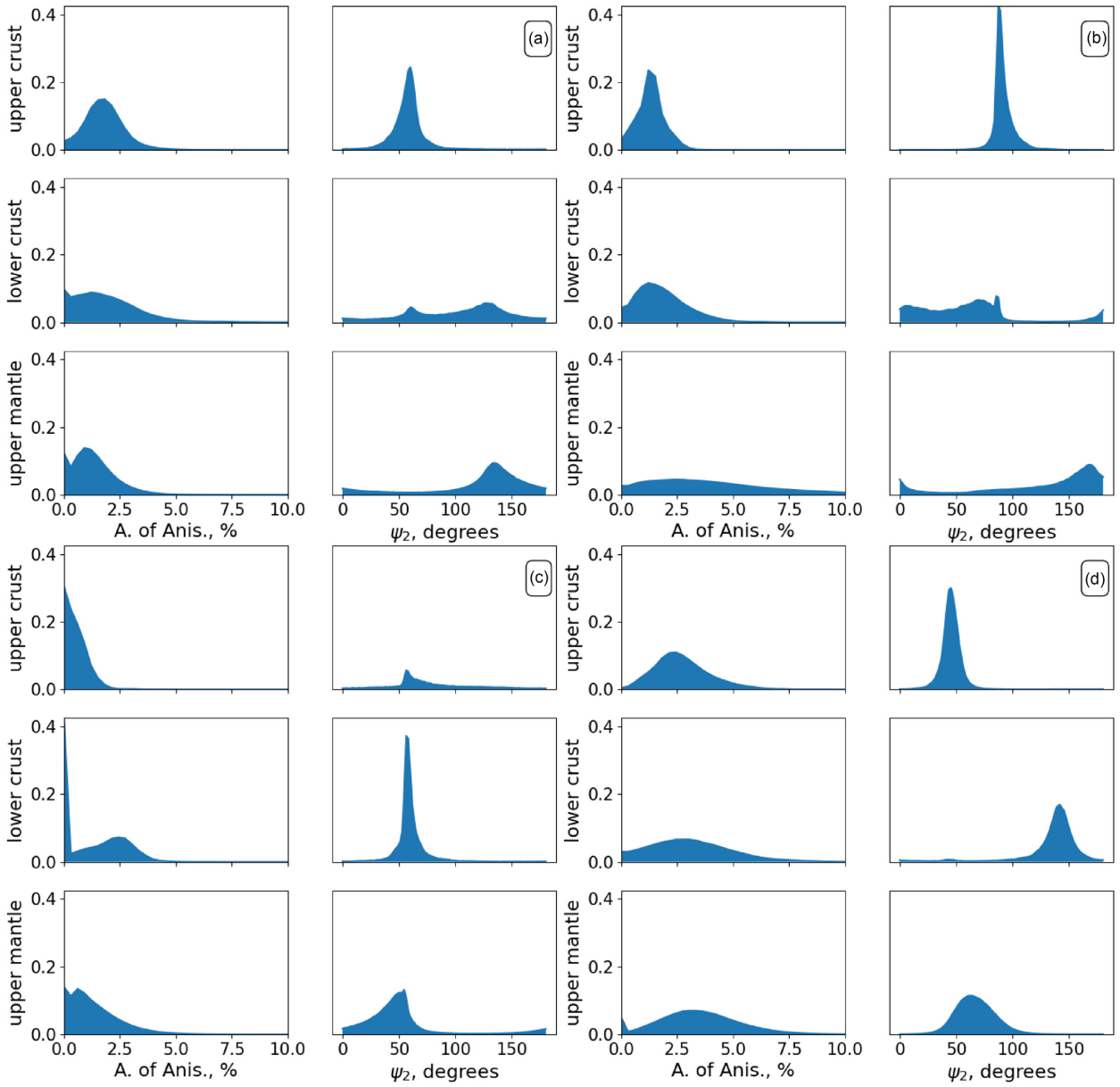

Figure 13. Marginal densities of δV_s and ψ_2 corresponding to locations 1, 5, 8 and 9, using amplitude bins of 0.3 per cent and angle (ψ_2) bins of 1.8°. The vertical scale is chosen such that the surface of the blue area is 1, that is the fraction of models with a given amplitude or (ψ_2) range corresponds to the blue area within that range.

5 DISCUSSION

5.1 Estimating anisotropy by beamforming applied to noise correlations

Our results show that beamforming applied to ambient noise correlations is a valuable complement to other methods to constrain surface wave azimuthal anisotropy as a function of period. Within a challenging study area, due to strong 3-D heterogeneities at short distances and varying network geometry over time, we were able to obtain maps of anisotropic parameters in the period range 15–70 s, with the number of measurements strongly depending on the period. The contribution of our method is particularly relevant at short periods (less than 40 s) where our method suffers less from multipathing and coda than studies based on teleseismic earthquakes (e.g. Deschamps *et al.* 2008; Adam & Lebedev 2012; Kolínský *et al.* 2020).

A wide range of methods are available for surface-wave imaging of isotropic structure. On the contrary, there are only a few methods available for anisotropic imaging at these periods, such as straight ray tomography of phase velocities (Fry *et al.* 2010), or eikonal tomography (Lin *et al.* 2009; Lin & Ritzwoller 2011; Kästle *et al.* 2021). With the recent eikonal results by Kästle *et al.* (2021), we have an opportunity to compare beamforming with eikonal tomography for anisotropic imaging across the greater Alpine area. Both methods are based on the same fundamental information, that is the Rayleigh-wave phase recorded at different periods for each station pair. The differences between the two methods reside in the way this information is treated. Rather than relying on a mathematical

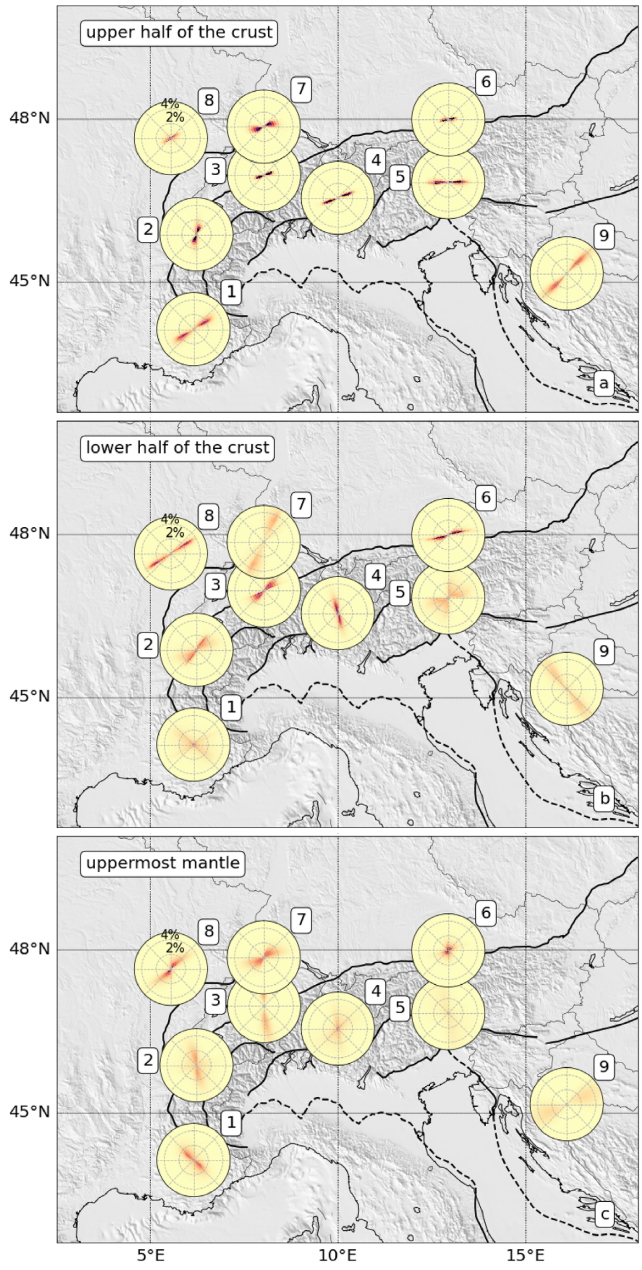

Figure 14. Probability distribution of integrated azimuthal anisotropy over three depth ranges: (a) upper half of the crust; (b) lower half of the crust and (c) uppermost mantle (Moho to 80 km depth). Each circle has the same layout as in Fig. 8, except that the outer circle corresponds to an anisotropy amplitude of 5 per cent. The colourscale is the same as in Fig. 8.

interpolation scheme of the phase information between seismic stations, our method is based on the hypothesis of local characteristics of the wavefield beneath a small study area (subarray), such as for example plane waves or, in our case, circular wave fronts.

Fig. 15 shows the comparison of our results with those obtained for eikonal tomography by Kästle *et al.* (2021) for three different periods. Overall, there is a good agreement on the fast axis directions, except at the border of the study area and for areas with small anisotropy amplitude, where the direction is poorly determined. Our amplitudes are almost always higher than those obtained by Kästle *et al.* (2021), with the differences being again especially large at the borders of the study area. At 15 s period (Fig. 15a), the two methods agree in most locations, both for the amplitude (A_2) and fast direction (θ_2). In particular, both methods yield smaller anisotropy amplitude (A_2) in the Alps as compared to peripheral areas. This has also been observed by Fry *et al.* (2010) within the Swiss Alps. A large area NW of the Alps is observed with very strong anisotropy, with the fast axis oriented NE–SW. This strong anisotropy tapers off towards the east, around 12–13°E. West of the Alps, moderate anisotropy with fast directions oriented E–W is observed. Note that the exact eastern limit of this area is different between the two studies. Strong anisotropy with fast directions oriented NE–SW is seen at the eastern extremity of the study area. Finally, both methods show moderate to strong anisotropy along the east coast of the Adriatic Sea (46°N–14°E), with ENE–WSW fast axes, although our measurements show higher amplitudes. There are also disagreements, mainly in peripheral areas with poor or no data coverage, such as the Adriatic Sea and in the Mediterranean Sea in the southeastern most part of the study area. For beamforming, we use virtual sources not only within the study area, but from all European stations around, effectively increasing constraints on anisotropy measurements at the edge of the array. This may yield stronger constraints on peripheral areas as compared to eikonal tomography, which could potentially be extended to use such additional data.

At 30 s period (see Fig. 15b), we are again mainly in agreement with Kästle *et al.* (2021) in terms of smaller anisotropy within the Alps both in terms of amplitudes and in terms of fast directions, and a large area of strong anisotropy with a NE–SW fast axis northwest of the Alps. Our study also confirms the Kästle *et al.* (2021) observations in the Apennines, with significant anisotropy and a fast direction oriented NE–SW. As Kästle *et al.* (2021), we do not obtain the same directions as Fry *et al.* (2010) for the Swiss part of the Alps. There are again areas of discrepancy on the periphery of the study area, as well as some internal parts, for example on the northern edge of the Po Plain, the northern part of the Apennines and in the northeastern part of the study area, for which we show examples of data in Fig. S10.

At longer period (40 s and above), the data scatter increases significantly, and at 40 and 50 s period A_1 increases. Our criteria on the uncertainty on A_2 and the ratio of A_1/A_2 mean that we have reliable estimates of A_2 and θ_2 for only a few subarrays (see Fig. 15c, and examples at 50 s period in Fig. S11). Kästle *et al.* (2021) covers the area fairly homogeneously, while our results on the contrary indicate that anisotropy estimates at long period using phase data from noise correlations may be unreliable in many locations. Kästle *et al.* (2021) also include a $\cos(4\theta)$ term in addition to $\cos(\theta)$ and $\cos(2\theta)$ terms. At 15 and 30 s period, the amplitude of the $\cos(4\theta)$ term they obtain is approximately 50 per cent of the amplitude of the $\cos(2\theta)$ term. At 50 s period, both terms are of similar magnitude. However, Kästle *et al.* (2021) argue against any mapping of the $\cos(4\theta)$ term into the $\cos(2\theta)$ term. Additionally, Figs 15, S10 and S11 show that adding a $\cos(4\theta)$ is not sufficient to explain an almost 90° discrepancy in fast direction. While differences in peripheral areas between the two methods can be understood in terms of data coverage, further investigation is needed to understand disagreements in the few interior locations where the two methods yield different results, and also to better understand the stability of each method at long periods.

From a practical point of view, beamforming has several advantages. First, each subarray is sufficiently small to avoid cycle skipping, as phase differences are measured only between the seismic stations of the array and not between (virtual) source and receiver. Second, our method makes it possible to minimize the influence

Table 1. Average anisotropy amplitudes and directions in all the areas and depths. per cent isotropic shows the percentage of models where the anisotropy is precisely zero over the whole layer.

Area	1	2	3	4	5	6	7	8	9
Lat	44.1	45.9	47.0	46.6	46.9	48.0	47.9	47.7	45.2
Lon	6.2	6.2	8.0	10.0	12.9	12.9	8.0	5.6	16.1
Moho (km)	32	32	39	49	51	32	32	27	33
ψ_2 (UC) (°)	58 ± 14	18 ± 20	73 ± 12	70 ± 8	91 ± 12	85 ± 18	75 ± 16	68 ± 45	46 ± 13
δV_s (UC, per cent)	1.7 ± 0.9	0.7 ± 0.5	0.6 ± 0.3	1.2 ± 0.4	1.4 ± 0.6	0.4 ± 0.3	1.0 ± 0.6	0.3 ± 0.5	2.7 ± 1.2
Per cent isotropic	0.	1.	1.	0.	0.	2.	0.	4.	0.
ψ_2 (LC) (°)	114 ± 64	56 ± 27	50 ± 20	166 ± 25	48 ± 33	75 ± 22	24 ± 14	59 ± 26	140 ± 20
δV_s (LC, per cent)	0.7 ± 1.7	1.0 ± 1.0	1.0 ± 0.7	1.2 ± 1.0	1.0 ± 1.1	1.0 ± 0.8	2.8 ± 1.4	1.2 ± 1.1	2.8 ± 2.0
Per cent isotropic	4.	14.	9.	1.	2.	28.	6.	40.	1.
ψ_2 (UM) (°)	141 ± 37	149 ± 50	172 ± 18	33 ± 73	156 ± 39	40 ± 88	60 ± 25	44 ± 30	66 ± 17
δV_s (UM, per cent)	0.9 ± 1.1	0.8 ± 1.4	2.8 ± 1.8	0.8 ± 2.0	2.5 ± 3.4	0.2 ± 0.6	1.0 ± 1.0	1.1 ± 1.2	3.0 ± 1.8
Percent isotropic	8.	9.	7.	14.	1.	8.	2.	9.	5.

of strong wavefield deformations over the scale of the whole study areas. When such deformations occur for a virtual source i at a given period and subarray, the quality measurement $d_{\max}$ will be small. The phase information from that virtual source is then down weighted in the linear regression that estimates the local azimuthal anisotropy from many virtual sources. The example in Fig. 5 shows that such local wave front deformations may occur when the waves propagate along strike of major lateral heterogeneities, resulting in strong azimuthal deviations. More subtle, but spatially coherent, wave front deformations can create bias in the anisotropy estimates, but they are approximately handled by estimating the $\cos(\theta)$ term (eq. 3). This term can also be estimated in eikonal tomography (e.g. Ritzwoller *et al.* 2011; Kästle *et al.* 2021)

One disadvantage of our implementation of the beamforming stems from the explicit geometrical handling. As we adapt the aperture of the subarrays to the wavelength, and relocate the information to the centre of mass, our sampling points are not the same for different periods, nor are they equally spaced across the study area for a given period. This means that to perform depth inversions, it is necessary to identify locations where the same subarray will yield well-constrained anisotropy estimates across a wide range of periods. Methods such as eikonal tomography suffer from the same limitation of changing resolution, but they will keep the location of observation constant across all of the period range.

5.2 Exploitation of Bayesian inversions results

It is not possible to directly interpret the maps of anisotropy in Fig. 11 in terms of depth variations. We therefore advocate that a depth inversion should be carried out whenever possible. While notoriously difficult for surface wave imaging, we also argue that it is possible to obtain relevant uncertainty estimates of Rayleigh wave anisotropy by carefully analysing errors and evaluating measurement quality at each step of the processing and inversion. This leads to a cascade of quality estimates which, combined, have the merit of eliminating outliers (by downweighting points with a small value of $d_{\max}$ in the beamforming), identifying and excluding problematic observation points (excluding points with a high value of A_1) and providing uncertainties (using bootstrap) of anisotropy parameters measured at a given period and subarray. These uncertainties can then be added as input to the depth inversion.

The Bayesian approach that we used for the depth inversion brings new challenges. For each of the nine identified subarrays, we obtain thousands of models which distribution approximates the posterior solution. For a given depth, our knowledge on shear wave anisotropy is poor, as a thin strongly anisotropic layer, and a thicker less anisotropic layer may yield the same effect on the period dependent values of A_2 and θ_2. Calculating, at each depth, the mean and standard deviation of inverted parameters is a classical way to exploit the results of a Bayesian inversion. But this approach does not entirely exploit the full level of information that a Bayesian inversion can provide. We therefore choose an alternative approach, by projecting each individual model into a lower dimensional parameter space, appropriate for visualization and exploitation of results. Knowing that upper crust, lower crust and uppermost mantle have different mechanisms for creating anisotropy, we simplified each of the models by integrating the anisotropy over each layer following Romanowicz & Yuan (2011). The large number of sampled velocity models allows us to approximate a complex posterior probability distribution, thus providing some estimate on the uncertainty on any parameter of interest (e.g. integrated anisotropy over a given depth range). This approach is different from a linear inversion based on a low number of parameters, as such regularized inversions do not take into account the non-linearity and non-uniqueness of the solution.

The outcome of this inversion process still remains complex to interpret, but can, for example, be visualized through plots of marginal densities (Fig. 13), or spatial plots of model parameters (Fig. 14), or mean values and standard deviations (Table 1). Each of these views provides complementary information. For example, the large standard deviations on the anisotropic parameters in the lower crust in location 1 (see Table 1) can be understood as a leakage of the anisotropy parameters from the upper crust and uppermost mantle into the lower crust (see Fig. 13a, lower crust). The resulting scatter in the plot in Fig. 14 represents the probable absence or very small anisotropy in the lower crust in location 1. All these representations are complementary and must be jointly analysed for a qualitative geodynamic interpretation.

5.3 Origins of lithospheric azimuthal anisotropy in the greater Alpine region

Overall, we observe little to no correlation between the anisotropy in each of the three layers (upper crust, lower crust and uppermost mantle). The origin of seismic anisotropy in the three layers are known to be different, with favoured mechanisms at large scale in the upper crust being oriented cracks or macroscopic orientation of anisotropic minerals (see, e.g. Keppler *et al.* 2021, for deformed

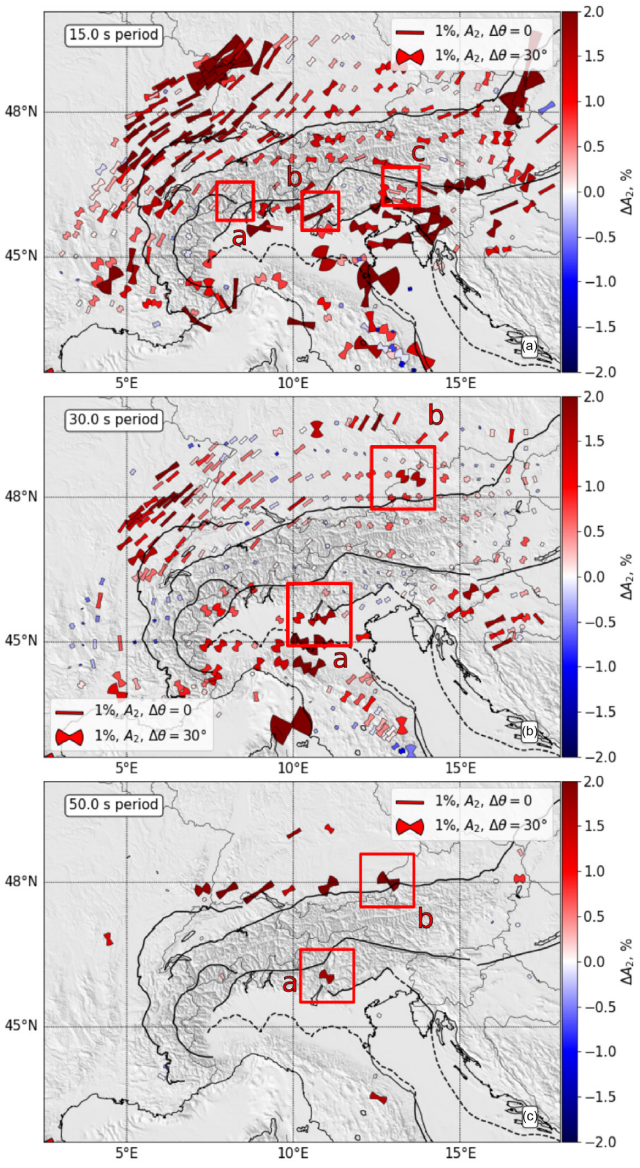

Figure 15. Map showing the differences between our work and the results obtained by Kästle *et al.* (2021) interpolated onto our subarray locations at 15, 30 and 50 s period. The length of the symbols indicates A_2 as obtained by this study, the width of the symbol the difference in anisotropy fast direction ($\Delta\theta$) and the colour the difference of the anisotropy amplitudes, both in percent (ΔA_2, and the direction is such as one edge indicates θ_2 according to our results and the other θ_2 from Kästle *et al.* (2021). For several locations (red boxes), we also show the fit of our anisotropy measurements to the data (see Fig. 6 for 15 s period and Figs S10 and S11 for 30 and 50 s period).

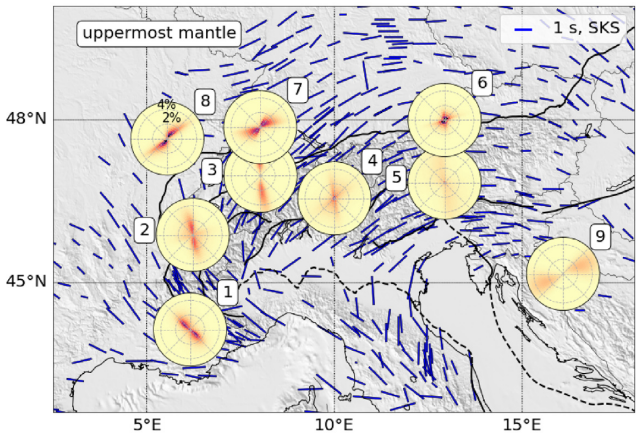

Figure 16. Anisotropy map of the upper mantle superimposed on XKS measurements (blue) by Hein *et al.* (2021).

upper crustal rocks in the Alps), in the lower crust crystallographic preferred orientation (CPO) of mica and amphibole (e.g. Tatham *et al.* 2008; Lloyd *et al.* 2009), and in the uppermost mantle CPO of olivine (e.g. Nicolas & Christensen 1987; Mainprice *et al.* 2000).

Surprisingly, though, only the upper crust shows a spatial pattern (see Fig. 14) which is coherent at the scale of the Alps, with a very high probability of anisotropy (>96 per cent) in all locations (see Table 1). In this layer, we observe fast directions that are approximately parallel to the Alps, and perpendicular to the stress field. While the fast direction in the southwesternmost part of the Alps (location 1 in Fig. 14) is not parallel to the Alps, the stress field also changes rapidly in this area. Our observations are coherent with anisotropy created through oriented cracks and fractures (Leary *et al.* 1990; Hudson *et al.* 1996; Heidbach *et al.* 2018). We speculate that the Cenozoic compression phase in the Alps has almost everywhere given rise to large-scale alignment processes in the upper crust.

In the lower crust, we observe significantly stronger differences between the different subarrays as compared to the upper crust, both in amplitude and directions, and two locations (6 and 8) having probabilities of 28 and 40 per cent of this layer being isotropic. The strongest lower-crustal anisotropy is observed northwest of the Alps (subarray 8, as well as to a lesser extent subarrays 2 and 3) with fast directions approximately oriented NE–SW. These directions can be explained by the imprint of late Carboniferous stretching in a major, lithospheric-scale shear zone that extended from southeastern France to the Bohemian massif (Guillot *et al.* 2009) with no subsequent change in anisotropic parameters, because this area remained unaffected by Alpine deformation. Location 7 is also part of the area potentially impacted by Variscan deformations, but may have been influenced by the opening of the Rhine Graben. We did not have sufficient long period observations in the Apennines to carry out depth inversions, but the decrease of amplitude and change of direction between 30 and 40 s period (see Fig. 11) tends to point to the lower crust as the source of the 30 s fast directions in the Apennines. This result is compatible with those of Alder *et al.* (2021) who observed strong radial anisotropy in the lower crust of the Apennines. Our results demonstrate that the anisotropy observed by Alder *et al.* (2021) cannot be explained by fine layering only, but must involve a mineralogical component, with fast axis that is perpendicular to the Apennines.

The layer that we call uppermost mantle, defined as the depths between Moho and 80 km, is part of the lithospheric mantle. Fig. 16 shows the comparison of our results with XKS measurements (Hein *et al.* 2021). There is little to no agreement (except locations 1 and 2) between our observations and XKS fast-velocity directions. This observation confirms previous suggestions that the XKS observations stem from below, either in the asthenosphere or in a combination of the asthenosphere and the detached slab, in the case of the eastern Alps or in toroidal flow in the asthenosphere around the Eurasian lithospheric slab north of the Alps Hein *et al.* (2021). It is possible that crustal anisotropy influences XKS measurements but because the anisotropy directions change strongly with depth in almost every location, the cumulative effect of the anisotropy we are

observing on the SKS data is expected to be very weak. Decoupling of deformation between lithospheric and asthenospheric layers has been observed in other mountain belts (Chen *et al.* 2016). All of the locations with depth inversions of Fig. 14 are located on European Lithosphere. A large-scale pattern would mean that the uppermost mantle could have been influenced by Alpine scale deformation in the lithosphere, due to for example subduction, slab break-offs, and slab roll back. However, no such large-scale pattern emerges, with the exception of some geographical coherency between locations 1–4, and a decrease of anisotropy amplitude further east (locations 5–6).

6 CONCLUSIONS

We show that beamforming on Rayleigh waves extracted by seismic noise correlations with the aim of extracting azimuthal anisotropy is possible, and that our implementation performs well in spite of time varying station geometry and strong lateral heterogeneities. We are able to carry out quality controls and error estimates at each step. The $\cos(\theta)$ term, created by lateral variations of isotropic parameters and indicative of potential bias on the azimuthal anisotropy, was particularly strong at 40 s and 50 s period and could in most locations be related to isotropic velocity gradients.

Our maps of Rayleigh wave azimuthal parameters at different periods largely confirm recent results by Kästle *et al.* (2021). We confirm the Fry *et al.* (2010) results at short periods in Switzerland but, as Kästle *et al.* (2021), we question the results by Fry *et al.* (2010) that indicate chain-perpendicular azimuthal anisotropy at periods between 24 and 40 s. We also have some locations where our results differ from those of Kästle *et al.* (2021). These differences can in the peripheral areas be explained by different data coverage, but they remain unexplained in a few internal parts of the study area.

The depth inversions demonstrate that the anisotropic structure at depth cannot easily be inferred from the results at individual periods. Exploiting the results of Bayesian inversions is complex, but we were able to reduce parameter space by vertical integration across three layers (upper and lower half of crust, and Moho to 80 km depth). With this procedure we were able to create complementary views on the density distribution of models. We advocate that such in-depth views are essential to fully benefit from the Bayesian framework in the case of non-linear and non-unique inversion problems.

In terms of the azimuthal anisotropy in the greater Alpine area, we observe that the upper half of the crust is the only layer which has a large-scale coherent azimuthal anisotropy at the scale of the Alps, while such large-scale patterns are absent in the lower half of the crust and the uppermost mantle. The logical conclusion is that the recent Alpine history has only overridden the anisotropic signature in the upper crust, and that the other layers carry the imprint of longer and/or older processes. There is no sign of coupling between lithospheric mantle and asthenosphere deformation, as there is little, if any, coherency between XKS observations and our observations for the uppermost mantle, which are restricted to the European lithosphere. Therefore, we confirm that XKS observations are related to deeper layers, the asthenosphere and/or subduction slabs. Finally, the radial anisotropy in the Apennines observed by Alder *et al.* (2021) is colocated with an area where we have indices of azimuthal anisotropy in the lower crust, with fast axis perpendicular to the Apennines. This finding confirms that the results by Alder *et al.* (2021) cannot be explained by fine layering in the lower crust.

For this work, we use data up to 70 s period, a choice which limits the number of locations where we can perform a depth inversion. However, based on this work and given the shape of the sensitivity kernels for anisotropy, we believe that by reducing the requirement for long periods, and sampling the shorter periods more densely, for example every 2 s, it should be possible to perform depth inversions at more locations so as to obtain a continuous coverage over the whole alpine area. We believe that this is a promising avenue for future work.

ACKNOWLEDGMENTS

We gratefully thank the operators of the European permanent seismic networks who make their data available through EIDA (http://www.orfeus-eu.org/eida). The Z3 network is operated by the AlpArray Seismic Network Team: Görgy Hetényi, Rafael Abreu, Ivo Allegretti, Maria-Theresia Apoloner, Coralie Aubert, Maxime Bes De Berc, Götz Bokelmann, Didier Brunel, Marco Capello, Martina Cărman, Adriano Cavaliere, Jérôme Chèze, Claudio Chiarabba, John Clinton, Glenn Cougoulat, Wayne Crawford, Luigia Cristiano, Tibor Czifra, Ezio D'Alema, Stefania Danesi, Romuald Daniel, Iva Dasović, Anne Deschamps, Jean-Xavier Dessa, Cécile Doubre, Sven Egdorf, ETHZ-SED Electronics Lab, Tomislav Fiket, Kasper Fischer, Wolfgang Friederich, Florian Fuchs, Sigward Funke, Domenico Giardini, Aladino Govoni, Zoltán Gráczer, Gidera Gröschl, Stefan Heimers, Ben Heit, Davorka Herak, Marijan Herak, Johann Huber, Dejan Jarić, Petr Jedlička, Yan Jia, Hélène Jund, Edi Kissling, Stefan Klingen, Bernhard Klotz, Petr Kolínský, Michael Korn, Josef Kotek, Lothar Kühne, Krešo Kuk, Jürgen Loos, Deny Malengros, Lucia Margheriti, Christophe Maron, Xavier Martin, Marco Massa, Francesco Mazzarini, Thomas Meier, Laurent Métral, Irene Molinari, Milena Moretti, Helena Munzarová, Anna Nardi, Jurij Pahor, Anne Paul, Catherine Péquegnat, Damiano Pesaresi, Davide Piccinini, Claudia Piromallo, Thomas Plenefisch, Jaroslava Plomerová, Silvia Pondrelli, Snježan Prevolnik, Roman Racine, Marc Régnier, Miriam Reiss, Joachim Ritter, Georg Rümpker, Simone Salimbeni, Detlef Schulte-Kortnack, Werner Scherer, Sven Schippkus, Vesna Šipka, Daniele Spallarossa, Kathrin Spieker, Josip Stipčević, Angelo Strollo, Bálint Süle, Gyöngyvér Szanyi, Eszter Szücs, Christine Thomas, Frederik Tilmann, Stefan Ueding, Massimiliano Vallocchia, Luděk Vecsey, René Voigt, Joachim Wassermann, Zoltán Wéber, Christian Weidle, Viktor Wesztergom, Gauthier Weyland, Stefan Wiemer, David Wolyniec, Thomas Zieke and Mladen Živvić. All data processing is carried out with python software, and the community software Obspy (Krischer *et al.* 2015) is used for many of the operations.

We thank Pierre Boué for his valuable help for the calculation of the correlations, Stéphane Guillot for his insights in the tectonic history of the Alpine area, Andrea Tomassi for her help for interpreting anisotropy measurements in terms of crystal orientations and Emanuel Kästle for our discussions on the measurement of anisotropy in the Alps.

We also thank two anonymous reviewers for their helpful comments. This manuscript was greatly improved thanks to their feedback.

This work is part of the project AlpArray-FR funded by Agence Nationale de la Recherche (contract ANR-15-CE31-0015), the Labex OSUG@2020 (Investissement d'Avenir, ANR-10-LABX-56) and by the European Research Council under the European Union Horizon 2020 research and innovation program (grant agreement 716542 – TRANSCALE).

REFERENCES

Adam, J. M.-C. & Lebedev, S., 2012. Azimuthal anisotropy beneath southern Africa from very broad-band surface-wave dispersion measurements, *Geophys. J. Int.,* **191**(1), 155–174.

Albuquerque Seismological Laboratory (ASL)/USGS, 1988. *Global Seismograph Network (GSN - IRIS/USGS),* International Federation of Digital Seismograph Networks, doi:10.7914/SN/IU.

Alder, C., Debayle, E., Bodin, T., Paul, A., Stehly, L. & Pedersen, H., the AlpArray Working Group, 2021. Evidence for radial anisotropy in the lower crust of the Apennines from Bayesian ambient noise tomography in Europe, *Geophys. J. Int.,* **226**(2), 941–967.

Almqvist, B.S.G. & Mainprice, D., 2017. Seismic properties and anisotropy of the continental crust: predictions based on mineral texture and rock microstructure, *Rev. Geophys.,* **55**(2), 367–433.

AlpArray Seismic Network, 2015. *AlpArray Seismic Network (AASN) Temporary Component,* AlpArray Working Group, doi:10.12686/alparray/z3_2015.

Alvizuri, C. & Tanimoto, T., 2011. Azimuthal anisotropy from array analysis of Rayleigh waves in Southern California: array analysis and azimuthal anisotropy, *Geophys. J. Int.,* **186**(3), 1135–1151.

Anderson, D.L., Minster, B. & Cole, D., 1974. The effect of oriented cracks on seismic velocities, *J. geophys. Res.,* **79**(26), 4011–4015.

Aristotle University Of Thessaloniki Seismological Network, 1981. *Permanent Regional Seismological Network Operated by the Aristotle University of Thessaloniki,* International Federation of Digital Seismograph Networks, doi:10.7914/SN/HT.

Backus, G.E., 1962. Long-wave elastic anisotropy produced by horizontal layering, *J. geophys. Res. (1896-1977),* **67**(11), 4427–4440.

Barruol, G., Bonnin, M., Pedersen, H., Bokelmann, G.H. & Tiberi, C., 2011. Belt-parallel mantle flow beneath a halted continental collision: the western alps, *Earth planet. Sci. Lett.,* **302**(3), 429–438.

Bodin, T. & Maupin, V., 2008. Resolution potential of surface wave phase velocity measurements at small arrays, *Geophys. J. Int.,* **172**(2), 698–706.

Bodin, T., Sambridge, M., Tkalčić, H., Arroucau, P., Gallagher, K. & Rawlinson, N., 2012. Transdimensional inversion of receiver functions and surface wave dispersion, *J. geophys. Res.,* **117**(B2), doi:10.1029/2011JB008560.

Bodin, T., Leiva, J., Romanowicz, B., Maupin, V. & Yuan, H., 2016. Imaging anisotropic layering with bayesian inversion of multiple data types, *Geophys. J. Int.,* **206**(1), 605–629.

Bogazici University Kandilli Observatory And Earthquake Research Institute, 2001. *Bogazici University Kandilli Observatory and Earthquake Research Institute,* International Federation of Digital Seismograph Networks, doi:10.7914/SN/KO.

Bokelmann, G., Qorbani, E. & Bianchi, I., 2013. Seismic anisotropy and large-scale deformation of the Eastern Alps, *Earth planet. Sci. Lett.,* **383,** 1–6.

Box, G.E. & Tiao, G.C., 1992. *Bayesian Inference in Statistical Analysis,* John Wiley and Sons, Ltd.

Campillo, M. & Paul, A., 2003. Long-range correlations in the diffuse seismic coda, *Science,* **299**(5606), 547–549.

Chen, H., Zhu, L. & Su, Y., 2016. Low velocity crustal flow and crust–mantle coupling mechanism in Yunnan, SE Tibet, revealed by 3D S-wave velocity and azimuthal anisotropy, *Tectonophysics,* **685,** 8–20.

Chevrot, S., Sylvander, M., Benahmed, S., Ponsolles, C., Lefèvre, J.M. & Paradis, D., 2007. Source locations of secondary microseisms in western Europe: evidence for both coastal and pelagic sources, *J. geophys. Res.,* **112**(B11), doi:10.1029/2007JB005059.

Chevrot, S. & Sylvander, M., RESIF, 2017. *Seismic Network x7:PYROPE PYRenean Observational Portable Experiment (RESIF-SISMOB),* RESIF - Réseau Sismologique et géodésique Français, doi:10.15778/RESIF.X72010.

Corinth Rift Laboratory Team, RESIF Datacenter, 2013. *CL - Corinth Rift Laboratory Seismological Network (CRLNET),* RESIF - Réseau Sismologique et géodésique Français, doi:10.15778/RESIF.CL.

Cotte, N., Pedersen, H.A., Campillo, M., Farra, V. & Cansi, Y., 2000. Off-great-circle propagation of intermediate-period surface waves observed on a dense array in the french alps, *Geophys. J. Int.,* **142**(3), 825–840.

Díaz, J., Gil, A. & Gallart, J., 2013. Uppermost mantle seismic velocity and anisotropy in the euro-mediterranean region from pn and sn tomography, *Geophys. J. Int.,* **192**(1), 310–325.

Delacou, B., Sue, C., Champagnac, J.-D. & Burkhard, M., 2004. Present-day geodynamics in the bend of the western and central Alps as constrained by earthquake analysis, *Geophys. J. Int.,* **158**(2), 753–774.

Department Of Earth And Environmental Sciences, Geophysical Observatory, University Of München, 2001. *BayernNetz,* International Federation of Digital Seismograph Networks, doi:10.7914/SN/BW.

Deschamps, A. & Beucler, E., 2016. *POSA Experiment,* RESIF - Réseau Sismologique et géodésique Français, doi:10.15778/RESIF.ZH2016.

Deschamps, F., Lebedev, S., Meier, T. & Trampert, J., 2008. Azimuthal anisotropy of rayleigh-wave phase velocities in the east-central united states, *Geophys. J. Int.,* **173**(3), 827–843.

Dias, N., Silveira, G. & Haberland, C., 2010. *Data of the Temporary Seismic WILAS Network,* GFZ Data Services, doi:10.14470/3N7565750319.

El-Sharkawy, A., Meier, T., Lebedev, S., Behrmann, J.H., Hamada, M., Cristiano, L., Weidle, C. & Köhn, D., 2020. The slab puzzle of the alpine-mediterranean region: Insights from a new, high-resolution, shear wave velocity model of the upper mantle, *Geochem. Geophys. Geosyst.,* **21**(8), e2020GC008993, doi:10.1029/2020GC008993.

ESI SAS (Earth Science Institute Of The Slovak Academy Of Sciences), 2004. *National Network of Seismic Stations of Slovakia,* Deutsches GeoForschungsZentrum GFZ, doi:10.14470/FX099882.

Essen, H.-H., Krüger, F., Dahm, T. & Grevemeyer, I., 2003. On the generation of secondary microseisms observed in northern and central europe, *J. geophys. Res.,* **108,** doi:10.1029/2002JB002338.

Faccenna, C., Becker, T.W., Miller, M.S., Serpelloni, E. & Willett, S.D., 2014. Isostasy, dynamic topography, and the elevation of the apennines of italy, *Earth planet. Sci. Lett.,* **407,** 163–174.

Federal Institute for Geosciences, Natural Resources (BGR), 1976. *German Regional Seismic Network (GRSN),* Federal Institute for Geosciences and Natural Resources (BGR), doi:10.25928/MBX6-HR74.

French Landslide Observatory – Seismological Datacenter / RESIF, 2006. *Observatoire multi-disciplinaire des instabilités de versants (OMIV),* RESIF - Réseau Sismologique et géodésique Français, doi:10.15778/RESIF.MT.

Friedrich Schiller University, Jena, 2009. *Thüringer Seismologisches Netz (TSN),* International Federation of Digital Seismograph Networks, doi:10.7914/SN/TH.

Froment, B., Campillo, M., Roux, P., Gouedard, P., Verdel, A. & Weaver, R.L., 2010. Estimation of the effect of nonisotropically distributed energy on the apparent arrival time in correlations, *Geophysics,* **75**(5), SA85–SA93.

Fry, B., Deschamps, F., Kissling, E., Stehly, L. & Giardini, D., 2010. Layered azimuthal anisotropy of Rayleigh wave phase velocities in the european alpine lithosphere inferred from ambient noise, *Earth planet. Sci. Lett.,* **297**(1), 95–102.

Gelman, A., Carlin, J.B., Stern, H.S. & Rubin, D.B., 1995. *Bayesian Data Analysis,* Chapman and Hall/CRC.

Geodesy National Institute Of Geophysics, 1980. *NatioNal Seismic Network of Bulgaria,* International Federation of Digital Seismograph Networks, doi:10.7914/SN/BS.

GEOFON Data Centre, 1993. *GEOFON Seismic Network,* Deutsches GeoForschungsZentrum GFZ, doi:10.14470/TR560404.

Geological And Seismological Institute Of Moldova, 2007. *Moldova Digital Seismic Network,* International Federation of Digital Seismograph Networks, doi:10.7914/SN/MD.

Geological Survey-Provincia Autonoma Di Trento, 1981. *Trentino Seismic Network,* International Federation of Digital Seismograph Networks, doi:10.7914/SN/ST.

Gerstoft, P. & Tanimoto, T., 2007. A year of microseisms in southern California, *Geophys. Res. Lett.,* **34**(20), doi:10.1029/2007GL031091.

Green, P.J., 1995. Reversible jump markov chain monte carlo computation and Bayesian model determination, *Biometrika,* **82**(4), 711–732.

Guéguen, P., Coutant, O. & Langlais, M., RESIF, 2017. *Maurienne Seismic Swarm 2017–2018,* RESIF - Réseau Sismologique et géodésique Français, doi:10.15778/RESIF.YW2017.

Guillot, S., di Paola, S., Ménot, R.-P., Ledru, P., Spalla, M.I., Gosso, G. & Schwartz, S., 2009. Suture zones and importance of strike-slip faulting for Variscan geodynamic reconstructions of the External Crystalline Massifs of the western Alps, *Bulletin de la Société Géologique de France,* **180**(6), 483–500.

Handy, M.R., Schmid, S.M., Bousquet, R., Kissling, E. & Bernoulli, D., 2010. Reconciling plate-tectonic reconstructions of alpine tethys with the geological-geophysical record of spreading and subduction in the alps, *Earth-Sci. Rev.,* **102**(3), 121–158.

Harmon, N., Rychert, C. & Gerstoft, P., 2010. Distribution of noise sources for seismic interferometry: distribution of noise sources for interferometry, *Geophys. J. Int.,* **183**(3), 1470–1484.

Hawkins, R., Bodin, T., Sambridge, M., Choblet, G. & Husson, L., 2019. Trans-dimensional surface reconstruction with different classes of parameterization, *Geochem. Geophys. Geosyst.,* **20**(1), 505–529.

Heidbach, O. *et al.*, 2018. The world stress map database release 2016: crustal stress pattern across scales, *Tectonophysics,* **744,** 484–498.

Hein, G., Kolínský, P., Bianchi, I. & Bokelmann, G., the AlpArray Working Group, 2021. Shear-wave splitting in the Alpine region, *Geophys. J. Int.,* **227**(3), 1996–2015.

Hetényi, G. *et al.*, 2018. The AlpArray seismic network: a large-scale European experiment to image the Alpine Orogen, *Surv. Geophys.,* **39**(5), 1009–1033.

Hudson, J., Liu, E. & Crampin, S., 1996. The mechanical properties of materials with interconnected cracks and pores, *Geophys. J. Int.,* **124**(1), 105–112.

INGV Seismological Data Centre, 2006. *Rete Sismica Nazionale (RSN),* Istituto Nazionale di Geofisica e Vulcanologia (INGV), Italy, doi:10.13127/SD/X0FXNH7QFY.

INSN, 1993. *Irish National Seismic Network, Operated by the Dublin Institute for Advanced Studies and supported by the Geological Survey Ireland,* International Federation of Digital Seismograph Networks, doi:10.7914/SN/EI.

Institut Cartogràfic I Geològic De Catalunya - Institut D'Estudis Catalans, 1984. *Catalan Seismic Network,* International Federation of Digital Seismograph Networks, doi:10.7914/SN/CA.

Institut de Physique du Globe de Paris (IPGP), Ecole et Observatoire des Sciences de la Terre de Strasbourg (EOST), 1982. *Geoscope, French Global Network of Broad Band Seismic Stations,* Institut de Physique du Globe de Paris (IPGP), doi:10.18715/GEOSCOPE.G.

Institute of Geophysics of the Academy of Sciences of the Czech Republic, 1973. *Czech Regional Seismic Network,* International Federation of Digital Seismograph Networks, doi:10.7914/SN/CZ.

Institute Of Geosciences, Energy, Water And Environment, 2002. *Albanian Seismological Network,* International Federation of Digital Seismograph Networks, doi:10.7914/SN/AC.

Institute Of Seismology, University Of Helsinki, 1980. *The Finnish National Seismic Network,* GFZ Data Services, doi:10.14470/UR044600.

Instituto Dom Luiz (IDL)-Faculdade De Ciências Da Universidade De Lisboa, 2003. *University of Lisbon Seismic Network,* International Federation of Digital Seismograph Networks, doi:10.7914/SN/LX.

Instituto Geografico Nacional, Spain, 1999. *Spanish Digital Seismic Network,* International Federation of Digital Seismograph Networks, doi:10.7914/SN/ES.

Instituto Português Do Mar E Da Atmosfera, I.P., 2006. *Portuguese National Seismic Network,* International Federation of Digital Seismograph Networks, doi:10.7914/SN/PM.

Jung, H. & Karato, S.-I., 2001. Water-induced fabric transitions in olivine, *Science,* **293**(5534), 1460–1463.

Juretzek, C. & Hadziioannou, C., 2016. Where do ocean microseisms come from? A study of Love-to-Rayleigh wave ratios, *J. geophys. Res.,* **121**(9), 6741–6756.

Kaminski, E. & Ribe, N.M., 2001. A kinematic model for recrystallization and texture development in olivine polycrystals, *Earth planet. Sci. Lett.,* **189**(3), 253–267.

Kedar, S., Longuet-Higgins, M., Webb, F., Graham, N., Clayton, R. & Jones, C., 2008. The origin of deep ocean microseisms in the North Atlantic Ocean, *Proc. R. Soc. Lond., A,* **464**(2091), 777–793.

Keppler, R., Vasin, R., Stipp, M., Lokajícek, T., Petruzálek, M. & Froitzheim, N., 2021. Elastic anisotropies of deformed upper crustal rocks in the alps, *Solid Earth,* **12**(10), 2303–2326.

KNMI, 1993. *Netherlands Seismic and Acoustic Network,* Royal Netherlands Meteorological Institute (KNMI), doi:10.21944/e970fd34-23b9-3411-b366-e4f72877d2c5.

Kolínský, P. & Bokelmann, G., the AlpArray Working Group, 2019. Arrival angles of teleseismic fundamental mode Rayleigh waves across the AlpArray, *Geophys. J. Int.,* **218**(1), 115–144.

Kolínský, P., Schneider, F.M. & Bokelmann, G., 2020. Surface wave diffraction pattern recorded on AlpArray: Cameroon volcanic line case study, *J. geophys. Res.,* **125**(7), e2019JB019102, doi:10.1029/2019JB019102.

Krischer, L., Megies, T., Barsch, R., Beyreuther, M., Lecocq, T., Caudron, C. & Wassermann, J., 2015. ObsPy: a bridge for seismology into the scientific Python ecosystem, *Comput. Sci. Discov.,* **8**(1), doi:10.1088/1749-4699/8/1/014003.

Kästle, E.D., Molinari, I., Boschi, L. & Kissling, E., the AlpArray Working Group, 2021. Azimuthal anisotropy from eikonal tomography: example from ambient-noise measurements in the AlpArray network, *Geophys. J. Int.,* **229**(1), 151–170.

Kövesligethy Radó Seismological Observatory (Geodetic And Geophysical Institute, Research Centre For Astronomy And Earth Sciences, Hungarian Academy Of Sciences (MTA CSFK GGI KRSZO)), 1992. *Hungarian National Seismological Network,* Deutsches GeoForschungsZentrum GFZ, doi:10.1088/1749-4699/8/1/014003.

Laboratorio Subterraneo De Canfranc, 2011. *LSC (Laboratorio Subterraneo Canfranc),* International Federation of Digital Seismograph Networks, doi:10.7914/SN/LC.

Landès, M., Hubans, F., Shapiro, N.M., Paul, A. & Campillo, M., 2010. Origin of deep ocean microseisms by using teleseismic body waves, *J. geophys. Res.,* **115**(B5), doi:10.1029/2009JB006918.

Leary, P.C., Crampin, S. & McEvilly, T.V., 1990. Seismic fracture anisotropy in the Earth's crust: an overview, *J. geophys. Res.,* **95**(B7), 11 105–11 114.

Leipzig University, 2001. *SXNET Saxon Seismic Network,* International Federation of Digital Seismograph Networks, doi:10.7914/SN/SX.

Löer, K., Riahi, N. & Saenger, E.H., 2018. Three-component ambient noise beamforming in the Parkfield area, *Geophys. J. Int.,* **213**(3), 1478–1491.

Lin, F.-C. & Ritzwoller, M.H., 2011. Helmholtz surface wave tomography for isotropic and azimuthally anisotropic structure, *Geophys. J. Int.,* **186**(3), 1104–1120.

Lin, F.-C., Ritzwoller, M.H. & Snieder, R., 2009. Eikonal tomography: surface wave tomography by phase front tracking across a regional broadband seismic array, *Geophys. J. Int.,* **177**(3), 1091–1110.

Lin, F.-C., Li, D., Clayton, R.W. & Hollis, D., 2013. High-resolution 3D shallow crustal structure in Long Beach, California: application of ambient noise tomography on a dense seismic array, *Geophysics,* **78**(4), Q45–Q56.

Link, F., Rümpker, G. & Kaviani, A., 2020. Simultaneous inversion for crustal thickness and anisotropy by multi-phase splitting analysis of receiver functions, *Geophys. J. Int.,* **223**(3), 2009–2026.

Lloyd, G.E., Butler, R. W.H., Casey, M. & Mainprice, D., 2009. Mica, deformation fabrics and the seismic properties of the continental crust, *Earth planet. Sci. Lett.,* **288**(1-2), 320–328.

Lu, L., Wang, K. & Ding, Z., 2018a. Effect of uneven noise source and/or station distribution on estimating the azimuth anisotropy of surface waves, *Earthq. Sci.,* **31**(4), 175–186.

Lu, Y., Stehly, L. & Paul, A., AlpArray Working Group, 2018b. High-resolution surface wave tomography of the European crust and uppermost mantle from ambient seismic noise, *Geophys. J. Int.,* **214**(2), 1136–1150.

Lu, Y., Stehly, L., Brossier, R. & Paul, A., 2020. Imaging Alpine crust using ambient noise wave-equation tomography, *Geophys. J. Int.,* **222**(1), 69–85.

Lu, Y., Pedersen, H.A. & Stehly, L., AlpArray Working Group, 2021. Mapping the seismic noise field in Europe: spatio-temporal variations in wavefield composition and noise source contributions, *Geophys. J. Int.,* **228**(1), 171–192.

Mainprice, D., Barruol, G. & Ismaïl, W.B., 2000. The Seismic anisotropy of the Earth's mantle: From single crystal to polycrystal, in *Geophysical Monograph Series,* Vol. **117,** pp. 237–264, eds Karato, S.-I., Forte, A., Liebermann, R., Masters, G. & Stixrude, L., American Geophysical Union.

Mathey, M. *et al.*, 2020. Present-day geodynamics of the Western Alps: new insights from earthquake mechanisms, *Solid Earth Discussions,* pp. 1–38, Copernicus GmbH, doi:10.5194/se-2020-196.

Mauerberger, A., Maupin, V., Gudmundsson, Ò. & Tilmann, F., 2021. Anomalous azimuthal variations with 360° periodicity of Rayleigh phase velocities observed in Scandinavia, *Geophys. J. Int.,* **224**(3), 1684–1704.

Maupin, V., 1985. Partial derivatives of surface wave phase velocities for flat anisotropic models, *Geophys. J. Int.,* **83**(2), 379–398.

Maupin, V., 2011. Upper-mantle structure in southern Norway from beamforming of Rayleigh wave data presenting multipathing, *Geophys. J. Int.,* **185**(2), 985–1002.

Maupin, V. & Park, J., 2015. Theory and observations—seismic anisotropy, in *Treatise on Geophysics,* pp. 277–305, ed. Schubert, G., Elsevier.

MedNet Project Partner Institutions, 1990. *Mediterranean Very Broadband Seismographic Network (MedNet),* Istituto Nazionale di Geofisica e Vulcanologia (INGV), doi:10.13127/SD/FBBBTDTD6Q.

Meier, T., Dietrich, K., Stöckhert, B. & Harjes, H.-P., 2004. One-dimensional models of shear wave velocity for the Eastern Mediterranean obtained from the inversion of Rayleigh wave phase velocities and tectonic implications, *Geophys. J. Int.,* **156**(1), 45–58.

Meissner, R., Mooney, W.D. & Artemieva, I., 2002. Seismic anisotropy and mantle creep in young orogens, *Geophys. J. Int.,* **149**(1), 1–14.

Montagner, J. & Nataf, H., 1986. A simple method for inverting the azimuthal anisotropy of surface-waves, *J. geophys. Res.,* **91,** 511–520.

Montagner, J.-P. & Tanimoto, T., 1991. Global upper mantle tomography of seismic velocities and anisotropies, *J. geophys. Res.,* **96,** 20 337–20 351.

National Institute For Earth Physics (NIEP Romania), 1994. *Romanian Seismic Network,* International Federation of Digital Seismograph Networks, doi:10.7914/SN/RO.

National Observatory Of Athens, Institute Of Geodynamics, 1997. *National Observatory of Athens Seismic Network,* International Federation of Digital Seismograph Networks, doi:10.7914/SN/HL.

Nicolas, A. & Christensen, N.I., 1987. *Formation of Anisotropy in Upper Mantle Peridotites—A Review,* pp. 111–123, American Geophysical Union (AGU).

Nocquet, J.-M. & Calais, E., 2004. Geodetic measurements of crustal deformation in the Western Mediterranean and Europe, *Pure appl. Geophys.,* **161**(3), 661–681.

Nouibat, A. *et al.*, 2022. Lithospheric transdimensional ambient-noise tomography of W-Europe: implications for crustal-scale geometry of the W-Alps, *Geophys. J. Int.,* **229**(2), 862–879.

Obrebski, M., Kiselev, S., Vinnik, L. & Montagner, J.-P., 2010. Anisotropic stratification beneath Africa from joint inversion of SKS and P receiver functions, *J. geophys. Res.,* **115**(B9), doi:10.1029/2009JB006923.

OGS (Istituto Nazionale Di Oceanografia E Di Geofisica Sperimentale), 2016. *North-East Italy Seismic Network,* International Federation of Digital Seismograph Networks, doi:10.7914/SN/OX.

OGS (Istituto Nazionale Di Oceanografia E Di Geofisica Sperimentale), University Of Trieste, 2002. *North-East Italy Broadband Network,* International Federation of Digital Seismograph Networks, doi:10.7914/SN/NI.

Paffrath, M. & Friederich, W., AlpArray Working Group, AlpArray-SWATH D Working Group, 2021. Teleseismic p waves at the alparray seismic network: wave fronts, absolute travel times and travel-time residuals, *Solid Earth,* **12**(7), 1635–1660.

Pedersen, H., Boué, P., Poli, P. & Colombi, A., 2015. Arrival angle anomalies of Rayleigh waves observed at a broadband array: a systematic study based on earthquake data, full waveform simulations and noise correlations, *Geophys. J. Int.,* **203**(3), 1626–1641.

Pedersen, H.A. & Krüger, F., the SVEKALAPKO Seismic Tomography Working Group, 2007. Influence of the seismic noise characteristics on noise correlations in the Baltic shield, *Geophys. J. Int.,* **168**(1), 197–210.

Poli, P., Pedersen, H.A. & Campillo, M., the POLENET/LAPNET Working Group, 2012. Emergence of body waves from cross-correlation of short period seismic noise, *Geophys. J. Int.,* **188**(2), 549–558.

Qorbani, E., Bianchi, I. & Bokelmann, G., 2015. Slab detachment under the eastern Alps seen by seismic anisotropy, *Earth planet. Sci. Lett.,* **409,** 96–108.

RESIF, 1995. *RESIF-RLBP French Broad-Band Network, RESIF-RAP Strong Motion Networkand Other Seismic Stations In Metropolitan France,* RESIF - Réseau Sismologique et géodésique Français, doi:10.15778/resif.fr.

RESIF, 2018. *CEA/DASE Broad-Band Permanent Network in Metropolitan France,* RESIF - Réseau Sismologique et géodésique Français, doi:10.15778/RESIF.RD.

Retailleau, L. & Gualtieri, L., 2019. Toward high-resolution period-dependent seismic monitoring of tropical cyclones, *Geophys. Res. Lett.,* **46**(3), 1329–1337.

Riahi, N. & Saenger, E.H., 2014. Rayleigh and love wave anisotropy in Southern California using seismic noise, *Geophys. Res. Lett.,* **41**(2), 363–369.

Riahi, N., Bokelmann, G., Sala, P. & Saenger, E.H., 2013. Time-lapse analysis of ambient surface wave anisotropy: a three-component array study above an underground gas storage, *J. geophys. Res.,* **118**(10), 5339–5351.

Ritzwoller, M.H., Lin, F.-C. & Shen, W., 2011. Ambient noise tomography with a large seismic array, *Compt. Rend. Geosci.,* **343**(8–9), 558–570.

Romanowicz, B. & Yuan, H., 2011. On the interpretation of SKS splitting measurements in the presence of several layers of anisotropy, *Geophys. J. Int.,* **188**(3), 1129–1140.

Rost, S. & Thomas, C., 2002. Array seismology: methods and applications, *Rev. Geophys.,* **40**(3), 2–1-2-27.

Royal Observatory Of Belgium, 1985. *Belgian Seismic Network,* International Federation of Digital Seismograph Networks, doi:10.7914/SN/BE.

Sabra, K.G., Gerstoft, P., Roux, P., Kuperman, W.A. & Fehler, M.C., 2005. Surface wave tomography from microseisms in Southern California, *Geophys. Res. Lett.,* **32**(14), doi:10.1029/2005GL023155.

Salimbeni, S. *et al.*, 2018. Active and fossil mantle flows in the western alpine region unravelled by seismic anisotropy analysis and high-resolution p wave tomography, *Tectonophysics,* **731–732,** 35–47.

San Fernando Royal Naval Observatory (ROA), Universidad Complutense De Madrid (UCM), Helmholtz-Zentrum Potsdam Deutsches GeoForschungsZentrum (GFZ), Universidade De Evora (UEVORA Portugal), Institute Scientifique Of RABAT (ISRABAT Morocco), 1996. *The Western Mediterranean Bb Seismic Network,* Deutsches GeoForschungsZentrum GFZ, doi:10.14470/JZ581150.

Schippkus, S., Zigone, D. & Bokelmann, G., AlpArray Working Group, ETHZ-Sed Electronics Lab, 2019. Azimuthal anisotropy in the wider Vienna basin region: a proxy for the present-day stress field and deformation, *Geophys. J. Int.,* **220**(3), 2056–2067.

Scripps Institution Of Oceanography, 1986. *IRIS/IDA Seismic Network,* International Federation of Digital Seismograph Networks, doi:10.7914/SN/II.

Sector For Seismology, Institute Of Hydrometeorology, 1982. *Montenegrin Seismic Network,* Sector for Seismology, Institute of Hydrometeorology and Seismology of Montenegro, doi:10.7914/SN/ME.

Segou, M., McCloskey, J., Baptie, B. & Hawthorn, D., 2016. *Armatrice Sequence International,* International Federation of Digital Seismograph Networks, doi:10.7914/SN/YR_2016.

Sens-Schönfelder, C. & Delatre, M., 2011. *Ketzin Seismic Monitoring Network,* GFZ Data Services, doi:10.14470/1T7566735694.

Shapiro, N.M. & Campillo, M., 2004. Emergence of broadband Rayleigh waves from correlations of the ambient seismic noise, *Geophys. Res. Lett.,* **31**(7), doi:10.1029/2004GL019491.

Shapiro, N.M., Campillo, M., Stehly, L. & Ritzwoller, M.H., 2005. High-resolution surface-wave tomography from ambient seismic noise, *Science,* **307**(5715), 1615–1618.

Slovenian Environment Agency, 2001. *Seismic Network of the Republic of Slovenia,* International Federation of Digital Seismograph Networks, doi:10.7914/SN/SL.

Smith, A. F.M., Cox, D.R. & Titterington, D.M., 1991. Bayesian computational methods, *Phil. Trans. R. Soc. Lond., A,* **337**(1647), 369–386.

Smith, M.L. & Dahlen, F.A., 1973. The azimuthal dependence of love and rayleigh wave propagation in a slightly anisotropic medium, *J. geophys. Res.,* **78**(17), 3321–3333.

Soergel, D., Pedersen, H.A., Stehly, L., Margerin, L. & Paul, A., AlpArray Working Group, 2020. Coda-Q in the 2.5 s–20 s period band from seismic noise—application to the greater Alpine area, *Geophys. J. Int.,* **220**(1), 202–217.

Soomro, R., Weidle, C., Cristiano, L., Lebedev, S. & Meier, T., PASSEQ Working Group, 2015. Phase velocities of rayleigh and love waves in central and northern europe from automated, broad-band, interstation measurements, *Geophys. J. Int.,* **204**(1), 517–534.

Spada, M., Bianchi, I., Kissling, E., Agostinetti, N.P. & Wiemer, S., 2013. Combining controlled-source seismology and receiver function information to derive 3-d moho topography for italy, *Geophys. J. Int.,* **194**(2), 1050–1068.

Stehly, L., Campillo, M. & Shapiro, N.M., 2006. A study of the seismic noise from its long-range correlation properties, *J. geophys. Res.,* **111**(B10), doi:10.1029/2005JB004237.

Stehly, L., Campillo, M., Froment, B. & Weaver, R.L., 2008. Reconstructing green's function by correlation of the coda of the correlation (C^3) of ambient seismic noise, *J. geophys. Res.,* **113**(B11), doi:10.1029/2008JB005693.

Swiss Seismological Service (SED) At ETH Zurich, 1983. *National Seismic Networks of Switzerland,* ETH Zürich, doi:10.12686/SED/NETWORKS/CH.

Tanimoto, T. & Prindle, K., 2007. Surface wave analysis with beamforming, *Earth, Planets Space,* **59**(5), 453–458.

Tatham, D.J., Lloyd, G.E., Butler, R. W.H. & Casey, M., 2008. Amphibole and lower crustal seismic properties, *Earth planet. Sci. Lett.,* **267**(1), 118–128.

Technological Educational Institute Of Crete, 2006. *Seismological Network of Crete,* International Federation of Digital Seismograph Networks, doi:10.7914/SN/HC.

University Of Athens, 2008. *University of Athens, Seismological Laboratory,* International Federation of Digital Seismograph Networks, doi:10.7914/SN/HA.

University Of Bari "Aldo Moro", 2013. *OTRIONS, Seismic Networks of Gargano Area (Italy),* International Federation of Digital Seismograph Networks, doi:10.7914/SN/OT.

University Of Genova, 1967. *Regional Seismic Network of North Western Italy,* International Federation of Digital Seismograph Networks, doi:10.7914/SN/GU.

University Of Patras, Geology Department, 2000. *PSLNET, Permanent Seismic Network Operated by the University of Patras, Greece,* International Federation of Digital Seismograph Networks, doi:10.7914/SN/HP.

University Of Trieste, 1993. *Friuli Venezia Giulia Accelerometric Network,* International Federation of Digital Seismograph Networks, doi:10.7914/SN/RF.

University Of Zagreb, 2001. *Croatian Seismograph Network,* International Federation of Digital Seismograph Networks, doi:10.7914/SN/CR.

Wüstefeld, A., Bokelmann, G., Barruol, G. & Montagner, J.-P., 2009. Identifying global seismic anisotropy patterns by correlating shear-wave splitting and surface-wave data, *Phys. Earth planet. Inter.,* **176**(3), 198–212.

Yao, H. & van der Hilst, R.D., 2009. Analysis of ambient noise energy distribution and phase velocity bias in ambient noise tomography, with application to SE tibet, *Geophys. J. Int.,* **179**(2), 1113–1132.

Yuan, H. & Bodin, T., 2018. A probabilistic shear wave velocity model of the crust in the central west australian craton constrained by transdimensional inversion of ambient noise dispersion, *Tectonics,* **37**(7), 1994–2012.

ZAMG-Zentralanstalt Für Meterologie Und Geodynamik, 1987. *Austrian Seismic Network,* International Federation of Digital Seismograph Networks, doi:10.7914/SN/OE.

SUPPORTING INFORMATION

Supplementary data are available at *GJI* online.

A. Data Availability

Figure S1. Uncertainty maps for θ_2 obtained from bootstrap at 15, 30 and 40 s period. The colour of each bar indicates the uncertainty on θ_2 at each period, its length the value of A_2 (expressed as a percentage of the isotropic velocity C_0) and its direction the value of θ_2. The uncertainty is generally below 5°, except where anisotropy is low.

Figure S2. Profiles corresponding to locations 1, 2, 3 and 4, similarly to Fig. 8.

Figure S3. Profiles corresponding to locations 5, 6, 7 and 8, similarly to Fig. 8.

Figure S4. Profile corresponding to location 9, similarly to Fig. 8.

Figure S5. Marginal distributions corresponding to locations 1, 2, 3 and 4, similarly to Fig. 8.

Figure S6. Marginal distributions corresponding to locations 5, 6, 7 and 8, similarly to Fig. 8.

Figure S7. Marginal distributions corresponding to location 9, similarly to Fig. 8.

Figure S8. Dispersion curve fit corresponding to locations 1, 2, 3, 4, 5 and 6, similarly to Fig. 9.

Figure S9. Dispersion curve fit corresponding to locations 7, 8 and 9, similarly to Fig. 9.

Figure S10. Anisotropy as observed at 30 s period in locations a and b of Fig. 15 (centre).

Figure S11. Anisotropy as observed at 50 s period in locations a and b of Fig. 15 (bottom).

Please note: Oxford University Press is not responsible for the content or functionality of any supporting materials supplied by the authors. Any queries (other than missing material) should be directed to the corresponding author for the paper.